Open access • Posted Content • DOI:10.1101/2020.09.09.290130

New mechanism of fibronectin fibril assembly revealed by live imaging and super-resolution microscopy — Source link

Darshika Tomer, Sudipto Munshi, Brianna E. Alexander, Brenda French ...+6 more authors

Institutions: Rutgers Biomedical and Health Sciences, Thomas Jefferson University, University of Pennsylvania, New Jersey Institute of Technology ...+1 more institutions

Published on: 10 Sep 2020 - bioRxiv (Cold Spring Harbor Laboratory)

Topics: Fibronectin fibril, Fibrillogenesis and Live cell imaging

New mechanism of fibronectin fibril assembly revealed by live imaging and super-resolution microscopy.

Darshika Tomer[1], Sudipto Munshi[2], Brianna E. Alexander[1,3], Brenda French[2], Pavan Vedula[4], Andrew House[5], Murat Guvendiren[5], Anna Kashina[4], Jean E. Schwarzbauer[6], and Sophie Astrof[1,*].

1. Department of Cell Biology and Molecular Medicine, Cardiovascular Research Institute, Rutgers Biomedical and Health Sciences, 185 South Orange Ave, Newark, NJ, 07103, USA.

2. Sidney Kimmel Medical College of Thomas Jefferson University, Philadelphia, PA, 19107, USA

3. Multidisciplinary PhD Program in Biomedical Sciences. Cell Biology, Neuroscience and Physiology track, Rutgers Biomedical and Health Sciences, Newark, NJ, 07103, USA.

4. Department of Biomedical Sciences, University of Pennsylvania, Philadelphia, PA 19104, USA

5. Otto H. York Chemical and Materials Engineering, Department of Biomedical Engineering, New Jersey Institute of Technology, Newark, NJ 07102, USA

6. Department of Molecular Biology, Princeton University, Princeton, New Jersey, USA

*Author for correspondence: Sophie Astrof, Ph.D.

Phone: 617-429-8295

E-mail: sophie.astrof@rutgers.edu

Abstract

- The regulation of cell fate decisions, morphogenesis, and responses to injury are intimately linked to the process of Fn1 fibrillogenesis. Live imaging and super-resolution microscopy revealed that Fn1 fibrils are not continuous. Instead, Fn1 fibrils arise from nanodomains containing multiple Fn1 dimers. As they move toward cell center, Fn1 nanodomains become organized into linear arrays with a spacing of 130 nm between the nanodomains, with little Fn1 in between; Fn1 nanodomain arrays are resistant to deoxycholate treatment demonstrating that these beaded assemblies are indeed mature Fn1 fibrils. FUD, a bacterial peptide that disrupts Fn1 fibrillogenesis, does not disrupt nanodomain formation; instead, it interferes with the organization of nanodomains into arrays. The nanodomain composition of Fn1 fibrils is observed in multiple contexts: in three-dimensional ECM *in vivo*, on substrata of different composition and stiffness, and is retained in the absence of cells. The modular architecture of Fn1 fibrils bears important implications for mechanisms of ECM remodeling and signal transduction.

Introduction

Fibronectin (Fn1) is a requisite component of extracellular matrix (ECM) necessary for embryogenesis and homeostasis (1). It is noteworthy that in the absence of Fn1 fibrillogenesis, the binding of Fn1 to cells is not sufficient to regulate key biological processes including those governing embryonic development, angiogenesis, vascular remodeling, or cartilage condensation (2-5). Therefore, understanding the mechanisms by which Fn1 proteins assemble into macromolecular fibrils is essential to gain insights into *in vivo* functions of Fn1. Fn1 fibrillogenesis occurs following the binding of secreted Fn1 homodimers to cell-surface integrins. Following integrin binding, intracellular cytoskeletal forces such as actomyosin contractility acting through integrins generate pulling forces on Fn1 dimers, exposing epitopes that promote Fn1 fibrillogenesis (6-10). At the cell biological level, the process of Fn1 fibrillogenesis is correlated with the formation of fibrillar adhesions, whereby mobile adhesions containing Fn1 and integrin $\alpha5\beta1$ translocate toward the nucleus resulting in elongated linear arrays termed focal and fibrillar adhesions, containing both Fn1 and intracellular cytoplasmic effectors linking Fn1 and actin cytoskeleton (11-16).

It has been thought that Fn1 fibrils arise following partial unfolding and alignment of Fn1 dimers in a periodic end-to-end fashion of alternating N- and C-termini, forming continuous fibers (17-19). However, this model is based on the analyses of fixed samples and electron microscopy wherein the exact composition of the fibrous material imaged could not be easily determined. To evaluate the process of fibrillogenesis in real time, we adopted a CRISPR/Cas9-mediated mutagenesis approach to generate fluorescently-labeled Fn1, subject to physiological regulation of expression and splicing. This approach has enabled us to visualize the initiation and progression of Fn1 fibrillogenesis over an extended period of time. Using live imaging and super resolution microscopy, we uncovered an unexpected mechanism of Fn1 fibrillogenesis. Our data demonstrate that Fn1 fibrils are composed of centripetally-

moving Fn1 nanodomains originating at cell periphery. As Fn1 nanodomains move toward the nucleus, they become arranged into progressively longer and longer arrays wherein nanodomains containing a high number of Fn1 dimers alternate with regions containing low or no Fn1. We show that the N-terminal Fn1 assembly region is not required for the formation of Fn1 nanodomains or their centripetal translocation. Instead, the N-terminus of Fn1 regulates the organization of Fn1 nanodomains into linear arrays. This model of fibrillogenesis integrates the process of fibrillogenesis with adhesion maturation and provides significant new insights into the mechanisms of ECM formation, remodeling, and signaling.

Results

While examining $Fn1^{+}$ ECM by confocal immunofluorescence microscopy in mouse embryos, we observed that Fn1 fibrils appeared discontinuous (**Fig. 1A-B**, arrows), containing regularly-spaced regions of high and low fluorescence intensity (**Fig. 1C, Movie 1**). This suggested that Fn1 fibrils consisted of regions with a high number of Fn1 dimers separated by regions containing a low number of Fn1 dimers (**Fig. 1C**). To test this hypothesis and to determine mechanisms regulating the formation of Fn1 fibrils, we employed a CRISPR/Cas9 knock-in strategy to modify the endogenous Fn1 locus by replacing the termination codon of Fn1 with a sequence encoding a fluorescent protein. This strategy has allowed to generate fluorescently-labeled Fn1 proteins subject to endogenous regulation (**Sup. Fig. 1A-B**), and enabled extended live imaging of Fn1 fibrillogenesis. Using this strategy, we obtained multiple independent lines of mouse embryo fibroblasts (MEFs) expressing Fn1-mEGFP, Fn1-mScarlet-I, Fn1-Neon Green, or Fn1-tdTomato fusion proteins (FP) generated by CRISPR/Cas9-mediated insertion. Western blots showed that FP fusions to Fn1 were specific: FPs were only fused to Fn1 as no other FP fusions were detected either by western blotting or immunofluorescence (IF) (**Sup. Fig. 2A-B**).

Deoxycholate (DOC) insolubility of Fn1 ECM is a classical biochemical assay for proteins stably incorporated into the assembled ECM (20-23). DOC assays demonstrated that the incorporation of Fn1-FPs into ECM was indistinguishable from wild-type, untagged Fn1 (**Sup. Fig. 2C**). To determine whether Fn1-FP proteins carried out the physiological functions of Fn1, we generated $Fn1^{mEGFP}$ knock-in mice. $Fn1^{mEGFP/mEGFP}$ homozygous knock-in animals are viable and fertile (**Sup. Fig. 1B** panels 4 and 5). Furthermore, Fn1-mEGFP proteins were expressed in the same pattern as total Fn1 protein (**Sup. Fig. 2d**) (24). Together, these studies demonstrated that Fn1-FP fusion proteins are suitable reagents for investigating mechanisms of Fn1 fibrillogenesis.

To visualize the process of fibrillogenesis in real time, we plated $Fn1^{mEGFP/+}$ MEFs on gelatin-coated cover glass and imaged cells 16 hours after plating using total internal reflection (TIRF) microscopy at the critical angle of incidence. These experiments showed that Fn1 fibrillogenesis initiated at cell periphery as distinct bright Fn1 densities that moved centripetally in parallel with F-actin and aligned into linear arrays of "beads" (arrows in **Movie 2**). TIRF imaging also showed that the domains of higher fluorescence intensity of Fn1 co-localized with integrin $\alpha5\beta1$ both in non-fibrillar adhesions (arrows in **Fig. 2A-A2**) and in fibrillar adhesions (arrows in **Fig. 2B-B2**), and that Fn1 and $\alpha5\beta1$ fibrillar adhesions are beaded (**Fig. 2B-B2**, arrows). We also observed the beaded architecture of Fn1 fibrils using an independent imaging method by employing Zeiss Airyscan (**Sup. Fig. 3**). Staining using monoclonal and polyclonal antibodies recognizing distinct and multiple epitopes in Fn1 resulted in the discontinuous appearance of Fn1 fibrils (**Fig. 3A1-C1**). Fn1 fibrils formed by cells plated on glass, gelatin, laminin 111 or vitronectin were beaded Fn1 fibrils (**Fig. 3**, and **Sup. Figs. 3-4**), and so were Fn1 fibrils in cell-free areas (**Fig. 3A, A1**) and between cells (**Fig. 3B-C**). In addition, the beaded appearance of Fn1 fibrils was observed when cells were plated on soft substrata such as hydrogels of variable stiffness (**Sup. Fig. 4C-D**). In the latter experiment,

Fn1 was detected by imaging the native fluorescence of Fn1-mEGFP, indicating that the beaded appearance of Fn1 fibrils was independent of antibody staining. Taken together, these studies indicated that the beaded appearance of Fn1 fibrils was a general feature of Fn1 ECM seen in 3D ECM *in vivo* and under different conditions *in vitro*.

To test the hypothesis that the "beads" in Fn1 strings were contiguous, cultures were treated with 2% DOC. 2% DOC treatment dissolves cell membranes and cytoplasmic components, leaving insoluble ECM devoid of cell contact (see **Movie 3** for time-laps of dissolution of cellular components, F-actin and DNA). This experiment showed that Fn1 fibrils in assembled ECM retained their beaded architecture in the absence of cell contact (**Fig. 3D**). Together, these data indicated that the beaded topology of Fn1 fibrils is a feature of physiological three-dimensional Fn1 ECM *in vivo* and suggested that the beads are contiguous.

To determine the relationship between the beaded architecture of Fn1 seen by diffraction-limited microscopy with Fn1 nanoarchitecture, we plated $Fn1^{mEGFP/+}$ MEFs on glass for 16 hours, then fixed and stained cells using a monoclonal antibody to the central region of Fn1. Fn1-mEGFP fluorescence was imaged in the TIRF mode at the critical angle of incidence, while the binding of the monoclonal αFn1 antibody was detected with Alexa Fluor-647-conjugated secondary antibody and imaged by Stochastic Optical Reconstruction Microscopy (STORM). STORM was performed by illuminating samples at the critical angle of incidence, as described in (25). Thin beaded fibrillar adhesions (arrow in **Fig. 4A**) were resolved by STORM (**Fig. 4B-B2**) to be arrays of regularly-spaced nanodomains that were symmetrical in x, y, and z dimensions (**Fig. 4B1, B2, B2'** and **Movie 4**). The space between nanodomains contained a few or no Fn1 localizations (**Fig. 4B2** and **Movie 4**).

Fn1 is a large, multi-domain, ~250 kDa glycoprotein secreted as a homodimer, wherein Fn1 subunits are linked in the anti-parallel orientation by two di-sulfide bonds at their C-termini

(1, 26). To investigate the relationship between the domain structure of Fn1 protein and the nanodomain architecture of Fn1 fibrils, we used antibodies to distinct parts of Fn1 protein (depicted in **Model 1** at the bottom of **Fig. 5**,) and STORM. For these experiments, wild-type and $Fn1^{mEGFP/+}$ MEFs were sparsely-plated in Ibidi 8-well glass-bottom chambers overnight, allowing to observe the structure of thin fibrils. Cells were then fixed and stained with antibodies recognizing different Fn1 epitopes: polyclonal rabbit antibodies raised to recognize the first six type III repeats of Fn1 (Fn1 $III_{1\text{-}6}$) (27) (**Fig. 5** column 1), a monoclonal antibody recognizing an epitope within the central region of Fn1 (**Fig. 5** columns 2, 4-5), polyclonal anti-serum 297.1 raised against the entire Fn1 protein (28) (**Fig. 5**, column 3), or polyclonal antibodies to GFP, recognizing the C-terminus of Fn1-mEGFP protein (**Fig. 6**, column 5). To maximize the labeling density, the polyclonal anti-Fn1 III_{1-6} and 297.1 antisera were used at a 40- and 4-fold higher concentrations than for routine immunofluorescence microscopy, respectively. Together with the use of excess secondary antibodies each conjugated to 3 – 6 molecules of Alexa-647, this approach maximizes the chance that all the epitopes recognized by the 1^{o} antibodies will be localized by STORM (25).

We first focused on the analyses of thin Fn1 fibrils like those marked by the arrows in (**Fig. 4A-B**) to study the initiation of fibril formation rather than fibril bundling or branching. Each antibody resulted in the detection of long characteristic Fn1 fibrils (**Fig. 5A-C**). Successive magnifications show that independent of the antibody used for staining, Fn1 fibrils contained linear arrays of nanodomains (thin arrows in **Fig. 5D, magnified in 5E**) separated by regions containing a small number or no Fn1 localizations (as in **Fig. 4, Movie 4**).

Surprisingly, staining with the polyclonal anti-serum 297.1 raised to the entire Fn1 and, presumably, recognizing multiple epitopes along Fn1, resulted in the same pattern of regularly-spaced nanodomains as staining with antibodies recognizing distinct parts of Fn1 molecule

(**Fig. 5,** column 3), suggesting that each Fn1 localization contained the entire Fn1 sequence, and that each nanodomain contained multiple Fn1 dimers.

These data are not consistent with previous models suggesting that Fn1 fibrils are composed of periodically aligned Fn1 dimers arranged in an end-to-end fashion of alternating N- and C-termini (17-19) (**Model 1** at the bottom of **Fig. 5**). Such periodic alignment of Fn1 dimers necessitates that staining using polyclonal antibodies would result in a uniform labeling of thin Fn1 fibrils, as depicted in **Model 1.** The dimers in the **Model 1** are aligned in an end-to-end fashion, according to the current Fn1 fibrillogenesis model, with the predicted overlap between the N-terminal Fn1 assembly domain (blue) and the first six type III repeats of Fn1 (red) (21)). If Fn1 fibrils, were indeed composed of continuous, linear arrays of dimers, the use of all four depicted in **Model 1** would be predicted to uniformly label Fn1 fibrils.

To test this prediction, we used $Fn1^{mEGFP/+}$ MEFs and a cocktail of four antibodies recognizing the beginning (αFn1 $III_{1\text{-}6}$), middle- (αFn1 monoclonal), and the end (αGFP) of Fn1-mEGFP protein in addition to all the epitopes recognized by 297.1 polyclonal antibody. The binding of all the antibodies in the cocktail was detected by a cocktail of secondary antibodies that were each conjugated to 3 – 6 molecules of Alexa-647 (**Fig. 5, column 7**). The nanoarchitecture of thin Fn1 fibrils, the nanodomain spacing (124 $\pm$ 25 nm between nanodomains in fibrils, on average), nanodomain size (average diameter 77 $\pm$ 18 nm), and the number of Fn1 localizations per nanodomain (average of 80 $\pm$ 43 localizations) detected by the cocktail of four antibodies were indistinguishable from those produced by each type of the antibody individually (**Fig. 5D – E**, quantified in **Fig. 5F-H** and **Tables 1 –3**). These results indicate that Fn1 fibrils are not uniform. Instead, our data show that Fn1 fibrils are arrays of nanodomains containing multiple Fn1 dimers separated by areas containing a few or no Fn1 molecules (**Fig.**

194 **5, Model 2**). The nanoarchitecture of Fn1 fibrils following the treatment with 2% DOC which
195 removes cells and cellular components, was similar to untreated fibrils (**Fig. 5,** columns 4 and
196 8, **Fig. 5F – H**). These data indicate that the nanodomain architecture is a feature of mature
197 Fn1 fibrils.
198
199 Fn1 nanodomains were also present outside of fibrils, we term them non-fibrillar nanodomains
200 (e.g. notched arrowheads in **Fig. 4**). About 3 – 5 such nanodomains are seen as a "bead" in
201 conventional diffraction-limited microscopy. Non-fibrillar Fn1 nanodomains contained a similar
202 number of Fn1 localizations per nanodomain and were of similar size compared with Fn1
203 nanodomains in fibrils (**Fig. 5H, Tables 2 – 3**). Staining using antibodies to endosomal and
204 lysosomal markers (Rab5 and LAMP1) showed no appreciable co-localization with Fn1
205 nanodomains (data not shown). Together with imaging using TIRF microscopy, these findings
206 indicated that Fn1 nanodomains in fibrils and non-fibrillar nanodomains are on the cell surface.
207 Non-fibrillar Fn1 nanodomains were present at cell periphery and throughout the cell surface,
208 but they were not organized into linear arrays and were spaced at an median distance of 329
209 nm (**Table 1**).
210 Live imaging experiments suggested that Fn1 fibrils form from centripetally-translocating
211 Fn1 nanodomains originating at cell periphery (**Movie 2**). To understand the relationship
212 between the observed nanodomain architecture of Fn1 fibrils and the process of fibrillogenesis,
213 we adopted a live imaging approach using $Fn1^{mEGFP/+}$ MEFs and inhibitors of fibrillogenesis.
214 Fn1 fibrillogenesis critically depends on the interactions mediated by the N-terminal assembly
215 domain of Fn1 (domains shaded in blue in **Model 1, Fig. 5**), and inhibitors that interfere with
216 these interactions block the formation of Fn1 fibrils (29-34). One such inhibitor is a 49-amino
217 acid peptide derived from *Streptococcus pyogenes* adhesin F1, termed the functional
218 upstream domain (FUD) (31). FUD binds the N-terminal assembly domain of Fn1 and
219 functions as a competitive inhibitor of Fn1-Fn1 interactions (31, 35). To determine how N-

terminal interactions regulate Fn1 fibrillogenesis, $Fn1^{mEGFP/+}$ MEFs were plated on glass for 4 hours, and then imaged for 15 – 18 hours either in the imaging medium alone, or in the medium containing either 225 nM FUD or 274 nM 11-IIIC, a 68 amino-acid control peptide that does not interfere with Fn1 fibrillogenesis (32, 36). Untreated cells or cells treated with the control peptide developed and accumulated long Fn1 fibrils (**Movie 5**). In contrast, treatment with FUD led to dismantling of the pre-existing Fn1 fibrils and inhibited the formation of new Fn1 fibrils (**Movie 6**). Instead of fibrils, cells cultured in the presence of FUD mainly contained centripetally-moving Fn1-mEGFP fluorescent "beads" that only rarely formed strings (**Movie 6**). These experiments suggested that FUD inhibits fibrillogenesis by interfering with the process by which Fn1 "beads" become arranged or connected into linear arrays. To test this hypothesis, $Fn1^{mEGFP/+}$ MEFs were plated for 16 hours in the continuous presence of either 225 nM FUD or 274 nM III-11C control peptides, or were left untreated. Cell were then fixed and stained without permeabilization using monoclonal anti-Fn1 antibodies which were detected with Alexa Fluor 647-conjugated secondary antibodies, and imaged at the critical angle of incidence by STORM at the excitation wavelength of 640 nm (25). This approach abolishes the detection of intracellular Fn1-mEGFP and maximizes the detection of cell-surface Fn1 due to the following: a) the absence of a detergent during fixation, staining and washing, b) detecting the emission of Alexa 647-conjugated antibodies at $\geq$ 670 nm, c) the use of oxygen scavengers in the STORM buffer that inhibits GFP fluorescence (37), and d) imaging at the critical angle of incidence to detect fluorescence in close proximity to the plasma membrane. These experiments demonstrated that the organization of nanodomains into linear arrays was lost upon incubation with FUD (compare **Fig. 6A, B, A1, B1** with **Fig. 6C, C1**). Non-fibrillar Fn1 nanodomains in cells treated with FUD had a similar number of Fn1 localizations per nanodomain, and were of similar sizes compared with fibrillar or non-fibrillar Fn1 nanodomains in untreated cells or cells incubated with the control peptide (**Fig. 6A2, 6B2, and 6C1-1**, quantified in Fig. **6D** and **Tables 2-3**). Taken together, these data indicate that

FUD does not interfere with the formation of Fn1 nanodomains but inhibits the organization of Fn1 nanodomains into linear arrays. Since Fn1 proteins lacking the N-terminal assembly domain do not form fibrils, our experiments suggest that interactions mediated by the N-terminal assembly domain of Fn1 are critical for the linking of Fn1 nanodomains into strings.

Discussion

In this manuscript, we describe the discovery of a novel mechanism underlying the process of Fn1 fibrillogenesis. We found that the three-dimensional beaded architecture of Fn1 ECM fibrils *in vivo* and in two-dimensional cell culture is due to the presence of Fn1 nanodomains, and showed that each Fn1 nanodomain is composed of multiple Fn1 dimers. Time-laps imaging by confocal and TIRF microscopy showed that Fn1 fibrillogenesis initiated at cell periphery, as bright fluorescent “beads” of Fn1-mEGFP moved centripetally in parallel with F-actin and became organized into linear arrays. Interestingly, the beaded appearance of focal and fibrillar adhesions has been noted before (13, 16), and the beaded architecture of cell adhesions can be seen in micrographs from multiple studies (e.g. Fig. 1C in (16), Fig 7a and Sup. Figs 1a and b in (38); Fig. 8B in (39); and lower left cell in Fig. 3A (40). However, the significance of these observations has not been investigated to the best of our knowledge. Fn1 domains and beaded strings in our movies resemble mobile, $Fn1^+$ adhesions similar to those described previously (13-16). The centripetal movement of these adhesions was dependent on the rearward actin flow, and the linkage of Fn1 to actin was mediated by integrin $\alpha5\beta1$ and tensin (13, 15, 16). Our TIRF microscopy experiments are consistent with these studies and show that integrin $\alpha5\beta1$ co-localizes with the regions of higher Fn1 intensity in fibrillar and non-fibrillar adhesions, and that $\alpha5\beta1^+$ focal and fibrillar adhesions are beaded. Taken together, our studies suggest that Fn1 fibrils arise from small mobile nanodomains containing $Fn1^+$ and integrin $\alpha5\beta1^+$ that move toward the cell’s center. This centripetal translocation of Fn1

nanodomains is coordinated with their organization into linear arrays, which become longer and longer as more nanodomains are added.

The number of Fn1 localizations in nanodomains is independent of the antibody type or amount used for staining, indicating that we are using saturating amounts of antibodies. Together with the preservation of the nanodomain architecture upon the treatment with DOC, our studies indicate that the non-uniform, beaded architecture is a salient feature of mature Fn1 fibrils. Two pieces of evidence suggest that Fn1 nanodomains in fibrils are contiguous: 1) the preservation of the linear organization and the nanoarchitecture of Fn1 fibrils after the treatment of cells with DOC which dissolves cell membranes, and 2) the presence of fibrous material between immunogold densities in electron micrographs (18, 19, 41). The sparsity of Fn1 localizations between Fn1 nanodomains in fibrils indicates that molecules other than or in addition to Fn1 participate in the linking of Fn1 nanodomains into strings.

FUD peptide specifically binds to the N-terminal assembly domain of Fn1 (35, 42) and acts as a competitive inhibitor of Fn1-Fn1 interactions (31, 43). In the absence of FUD, individual fibrils in an established matrix are stable and can be tracked for over 16 hours (data not shown). When FUD is added to cells, it specifically co-localizes with Fn1 fibrils and dismantles the mature Fn1 ECM (31, 34), suggesting that the linear arrangement of Fn1 nanodomains in the fibrillar ECM is maintained through dynamic interactions mediated at least in part by the Fn1 N-terminal assembly domain. Our live imaging experiments demonstrated that in addition to dismantling pre-existing fibrils, FUD effectively blocks their de-novo formation. STORM showed that FUD does not affect the formation of Fn1 nanodomains, instead, it blocks the organization of Fn1 nanodomains into linear arrays. Together, these data suggest that FUD may block the dynamic interactions between the N-terminal Fn1 assembly domain and the factor(s) linking Fn1 nanodomains into fibrils.

297

298 The beaded architecture of Fn1 ECM has important implications for the mechanisms of ECM
299 formation, remodeling and signal transduction. The tensile strength of knotted strings is
300 significantly lower than that of strings with uniformly-aligned fibers (44, 45), thus the beaded
301 architecture of Fn1 fibrils may facilitate their rupture under strain (46). The non-uniform,
302 nanodomain architecture of Fn1 may facilitate the accessibility of Fn1 fibrils to matrix
303 metalloproteases. In this model, degradation of Fn1 fibrils by metalloproteases may be
304 accomplished by cleaving between Fn1 nanodomains facilitating ECM remodeling. Finally, Fn1
305 is known to bind growth factors (47-49), and cell adhesion to ECM is known to orchestrate
306 growth factor signaling (50). Thus, Fn1 nanodomains could serve as platforms for the binding
307 and presentation of concentrated packets of growth factors to cells, the organization of Fn1
308 nanodomains into closely-spaced arrays could further facilitate clustering and signaling by
309 growth factor receptors.

310

311 **Acknowledgements**

312 We thank Richard Hynes and Nathan Astrof for insightful discussions and careful reading of
313 the manuscript, Sydney Astrof for help with data entry and encouragement, Patrick Murphy for
314 endothelial cells, Richard Hynes for the gift of 297.1 antibody, and Tung Chan for help with
315 setting up Western Blotting using ProteinSimple.

316

317 **Sources of Funding** This work was supported by the funding from the National Heart, Lung,
318 and Blood Institute of the NIH R01 HL103920 and R01 HL134935 to SA, by the NIH Office of
319 the Director R21 OD025323-01 to SA, by the pre-doctoral fellowship F31HL151046 to BEA, by
320 the National Institute of General Medicine R35GM122505 to AK, by the National Institute of
321 Arthritis and Musculoskeletal and Skin Diseases R01 AR073236 to JES, by the Faculty Seed
322 Grant from the Center for Engineering MechanoBiology (CEMB), an NSF Science and

Technology Center, under grant agreement CMMI: 15-48571. Any opinions, findings, and conclusions or recommendations expressed in this material are those of the authors and do not necessarily reflect the views of the National Science Foundation.

Materials and Methods

Generation Fn1-fluorescent protein targeting constructs

Sequences of monomeric (m) green fluorescent protein (GFP), mNeonGreen, mScarlet-I, and tdTomato were obtained from FPbase (https://www.fpbase.org). The sequence encoding one of the above fluorescent proteins (FPs) was knocked into the Fn1 locus following the last coding exon of mouse Fn1, and separated from the last coding amino acid by a flexible, proline-rich linker, PPPELLGGP (51). Targeting was achieved by CRISPR/Cas9 (52). The sequence of the guide RNA was chosen and off-target sites were identified using GuideScan and Off-Spotter software (53, 54). The guide RNA (gRNA) sequence 5'-AGC GGC ATG AAG CAC TCA AT-3' targeting the last coding exon of *Fn1* was subcloned downstream the U6 promoter into the PX459 vector (Addgene, cat # 62988) encoding the Cas9-2A-Puromycin cassette (52). The homology-directed repair (HDR) template was constructed using pBS-KS vector (Sup. Fig. 1a). The sequence of the last coding exon of *Fn1* 5'-AACGTAAATTGCCCCATTGAGTGCTTCATGCCGCTAGATGTGCAAGCTGACAGAGACGATTCTCGAGAG-3' was modified to 5'-AACGTAAATTGCCCCATcGAaTGCTTCATGCCGCTAGATGTGCAAGCTGACAGAGACGATTCTCGAGAG-3' in the HDR template by introducing silent mutations (underlined) to prevent targeting of the template by the gRNA. Homology arm 1 contained 677 bp encoding exon #45, intron, and a portion of the last exon (#46), of the transcript *ENSMUST00000055226.12*. Homology arm 2 encoded 1739 bp immediately downstream of the *Fn1* termination codon and included the unmodified 3'UTR of Fn1. Knockin Fn1$^{mEGFP/+}$ mice were generated by

Biocytogen using the same HDR construct and a longer gRNA, 5'-TAG CGG CAT GAA GCA CTC AAT GG-3',

targeting the same sequence in the last coding exon (differences between the two gRNAs are underlined). Targeting was confirmed by sequencing and Southern Blotting (Sub. Fig. 1b). 500 bp around each of the top ten predicted off-target sites were sequenced and no mutations were found in the founder mice. Mice containing correctly-targeted *Fn1* locus were used to establish living colonies of $Fn1^{mEGFP/mEGFP}$ animals. Mice were housed in an AAALAC-approved barrier facility. All experimental procedures were approved by the Institutional Animal Care and Use Committee of Rutgers University and conducted in accordance with the Federal guidelines for the humane care of animals.

Generation of Fn1-FP-expressing cell lines

Mouse embryonic fibroblasts (MEFs) were isolated from embryonic day (E) 13.5 embryos derived from the C57BL/6J strain (Jackson Labs, stock # 664) according to established protocols (55) and cultured in high-glucose Dulbecco's Modified Eagle Medium (DMEM, Corning, cat # 10-013-CV) supplemented with 10% v/v fetal bovine serum (Gemini Biosciences, cat # 100-106), 1% v/v penicillin/streptomycin solution (GE Healthcare, cat #SV30010), 1% v/v L-glutamine (Gibco, cat # 35050-061). We refer to this as complete medium henceforth in the methods. CRISPR targeting was performed by transfecting the PX459 plasmid encoding Fn1 gRNA and the HDR template using lipofectamine 3000, as described (52). For all other experiments, MEFs expressing Fn1-mEGFP proteins were generated from E13.5 $Fn1^{mEGFP/+}$ embryos. Wild-type MEFs were isolated from the littermates of $Fn1^{mEGFP/+}$ embryos.

Analysis of Fn1 matrix assembly

Matrix Assembly was performed according to the established protocols (22). MEFs were plated in 6-well dishes (9 cm^2 growth area) at a density of 2 × 10^5 cells per well for 48 h, in complete medium and incubated under sterile conditions at 37°C, 5% CO2. Cells were washed twice with ice cold PBS (supplemented with Mg^{2+} and Ca^{2+}), scraped with a cell scraper and lysed with either 500 μl RIPA lysis buffer pH 8.0 (50 mM Tris-Cl, 150 mM NaCl, 2 mM EDTA, 1% v/v NP-40, 0.5% w/v sodium deoxycholate, 0.1% w/v SDS, 1X protease inhibitor cocktail (Cell Signaling Technology, cat # 5871), or DOC lysis buffer, pH 8.8 (20 mM Tris-Cl, 2 mM EDTA, 2% w/v sodium deoxycholate, 1X protease inhibitor cocktail (Cell Signaling Technology, 5871). Extracts were carefully transferred to Eppendorf tubes containing 1 μl (250 units) Benzonase® Nuclease (Sigma-Aldrich, E1014), mixed by inverting a few times and incubated at 37 °C for 15 mins. The samples were then centrifuged at 16,000 × g for 15 min at 4 °C. For cells lysed with DOC lysis buffer, the supernatant containing DOC-soluble material was carefully removed, and the pellet containing the DOC-insoluble material was resuspended in 100 μl SDS solubilization buffer, pH8.8 (20 mM Tris-Cl, 2 mM EDTA, 1% w/v SDS, 1X protease inhibitor cocktail (Cell Signaling Technology, 5871). The DOC-insoluble pellet was thoroughly dissolved by heating the sample to 95 °C and vortexing. All samples were aliquoted and stored at -80 °C until further use. Prior to quantification of Fn1 in the samples, the total protein concentration of the RIPA and DOC lysates was determined using the BCA protein assay (Pierce™ BCA Protein Assay Kit, 23225). Fn1 and Fn1-FP fusion proteins were resolved using 66-440 kDa Wes separation module (ProteinSimple, SM-W007). Primary antibodies were used at the following dilutions: anti-total Fn1 – 1:1000 (Abcam, ab199056), anti-GFP – 1:1000 (Roche, 11814460001), anti-mCherry – 1:1000 (Abcam, 167453). Primary antibodies were detected using horseradish peroxidase-conjugated secondary antibodies (anti-Rabbit Detection Module ProteinSimple, DM-001), and chemiluminescence was quantified using the

Compass for SW software (v3.1.8). Prior to running experimental samples, care was taken to optimize the dilutions of lysates to be within the linear range of the detection.

Chemicals and reagents

Cells were grown in complete medium consisting of high-glucose Dulbecco's Modified Eagle Medium (DMEM, Corning, cat # 10-013-CV) supplemented with 10% v/v fetal bovine serum (Gemini Biosciences, cat # 100-106), 1% v/v penicillin/streptomycin solution (GE Healthcare, cat #SV30010), 1% v/v L-glutamine (Gibco, cat # 35050-061). During live imaging cells were incubated in FluoroBrite DMEM (Thermo Fisher Scientific, catalog # A1896701) supplemented with 2% v/v fetal bovine serum (Gemini Biosciences 100-106), 1% v/v penicillin/streptomycin solution (GE Healthcare, SV30010), 1% v/v L-glutamine (Gibco 35050-061). We refer to this as imaging medium in the methods henceforth. The pH of the imaging medium was 8.14. FUD and III-11C peptides were generated as described (31, 36) and stored in PBS at -80^{o} C. 4% DOC solution was prepared by dissolving 0.4 g deoxycholate salt (Sigma, catalog # D6750) in 10 ml of imaging medium; the solution was then vortexed and filter sterilized. The pH of the final solution was 8.01. 16% paraformaldehyde (PFA) (Electron microscopy Sciences; catalog # 50-980-487) was diluted in 1x PBS to prepare 4% PFA. The 4% PFA solution was aliquoted into 1 ml microfuge tubes, stored at -80^{o} C, and thawed at 37^{o} C immediately before use. Triton X-100 (100X stock, Sigma-Aldrich, catalog # T-8787) was used to prepare 1X PBST by diluting in 10X PBS (VWR, catalog # 76180-740). Blocking buffer was prepared by adding 5% Donkey serum (Sigma-Aldrich, catalog # D9663) to 1X PBST. 5 mg/ml stock of DAPI (Fisher Scientific, cat #D3571) was prepared in water and used at 1:300 dilution. Stain Buffer (cat # 554656 BD Pharmingen) was used for antibody dilutions and washing of cells that were stained without permeabilization. Hoechst 33342 Trihydrochloride, Thermo Fisher, catalog # H1399, Stock- 10mg/ml, was used for labelling live MEFs at 1:300 dilution. In live MEFs, F-actin was labelled using SiR actin (cat# CY-SC001 used at 1 μM final concentration).

mCardinal-Lifeact-7 was a gift from Michael Davidson (Addgene plasmid # 54663 ; http://n2t.net/addgene:54663 ; RRID:Addgene_54663). Vectashield antifade mounting medium (Vectorlabs, catalog # H-1000), was used for cover slipping. STORM buffer was prepared using 50 mM Tris-HCl (fisher scientific, catalog # T-395-1), pH 8.0, 10 mM NaCl (Sigma-Aldrich, catalog # S-7653), 10% glucose (Sigma- Aldrich, catalog # G8270), 0.5 mg/ml glucose oxidase (Sigma- Aldrich, catalog # G2133), 40 μg/ml catalase (Sigma- Aldrich, catalog # C40), 10 mM mercaptoethylamine (MEA, Sigma-Aldrich, catalog # 30070), according to (56).

Cell plating and chambers

All live imaging and STORM experiments were performed using Ibidi glass bottom 8-well chambers (catalog # 80827) or MatTek round glass bottom dishes (catalog # P35G-1.5-14-C). For imaging fixed cells, cells were plated on #1.5 round glass coverslips (Electron Microscopy Sciences. Catalog # 72230-01). Coverslips were used either without coating or were coated with the following ECM proteins: gelatin (Sigma Aldrich, catalog # G2500) (stock 0.1% in distilled water), vitronectin (Sigma Aldrich, catalog # SRP3186; stock solution was prepared as 200μg/ml in 0.1% BSA and water) and laminin (R&D systems, catalog # 3400-010-02, stock 1 mg/ml was pipeted into 10ul aliquots and stored at -80^{O}C). To coat with gelatin, glass surfaces were incubated with the 0.1% gelatin solution for 5 min at room temperature (rt). To coat with vitronectin or laminin, glass surfaces were incubated at 37^{o} C for 1 hr in 20 μg/ml of either vitronectin or laminin, excess liquid was removed, cover slips were rinsed once with 1X PBS, and blocked with 10 μg/ml heat denatured BSA for 30 min before plating cells (14). Cells were grown in complete medium. During live imaging cells were incubated in imaging medium.

Antibodies

All primary antibodies were checked for specificity on genetically-null tissues: Fn1-null tissue sections obtained from Fn1-null embryos were used to assay the specificity of each of the anti-

Fn1 antibodies; Tissues isolated from GFP-null, Itga5-null, and mCherry-null embryos were used to check the specificity of anti-GFP, anti-Itga5, and anti-mCherry antibodies. For each of the antibodies, staining of control tissues resulted in no more fluorescent signal than the background fluorescence produced by the use of secondary antibodies only.

Antibodies

Primary Antibodies (Ab)	Source, catalog #, concentration	Dilution / ng used per staining
tFn monoclonal Ab	Abcam, cat # 199056, 0.429 mg/ml	1:300 for STORM, 429 ng
tFn polyclonal Ab, 297.1 serum	Richard Hynes lab	1:2000 for IF, 1:500 for STORM
Fn1 N-term, R184 serum	Jean Schwarzbauer's lab	1:2000 for IF, 1:25 for STORM
GFP	Aves lab, cat# GFP-1010, 30 μg/ml	1:300 for STORM / 30 ng
Itgα5	BD biosciences, cat # 553319	1:100
mCherry	Abcam, cat # ab167453	1:100

Secondary Antibodies	Source, catalog #, concentration	Dilution/ μg of antibody in staining solution)
donkey anti-rabbit Alexa Fluor 647	Thermo Fisher Scientific, A-31573, 2 mg/ml	1:300 / 2 μg

donkey anti-mouse Alexa Fluor 555	Thermo Fisher Scientific, A-31570, 2 mg/ml	1:300 / 2 μg
donkey anti-rat Alexa Fluor 555	Jackson Immunoresearch, 712-166-150, 1.5mg/ml	1:300 / 1.5 μg
donkey anti-chicken Alexa Fluor 488	Jackson Immunoresearch, 703-546-155, 1.5mg/ml	1:300 / 1.5 μg
donkey anti-chicken Alexa Fluor 647	Jackson Immunoresearch, 703-606-155, 1.5mg/ml	1:300 / 1.5 μg

Cell culture and treatments

MEFs were maintained by plating on 25 cm^2 dishes (25 cm^2 growth area) in complete medium and incubated under sterile conditions at 37°C, 5% CO_2. For FUD and III-11C treatment $Fn1^{mEGFP/+}$ MEFs were plated in 8-well glass Ibidi dishes (1 cm^2 growth area) without coating at a density of $0.6x10^4$ cells/well in complete medium. After 5 hours, DMEM was removed and cells were rinsed once with 1X PBS. Subsequently, the medium was changed to imaging medium. For FUD experiments, imaging medium was supplemented either with 225 nM FUD or 274 nM of control III-11C peptide. Untreated wells contained cells incubated with imaging medium. Following the addition of the imaging medium (with or without the peptides), the chamber was immediately set up for live imaging under in the humidified Tokai Hit stage-top incubator at 37°C, 5% CO_2.

In order to enrich for non-fibrillar nanodomains, $Fn1^{mEGFP/+}$ MEFs were plated in 8 well glass Ibidi dishes (1 cm^2 growth area) without coating. Cell were plated at the density of $0.6x10^4$ cells/well in imaging medium with or without FUD (225 nM) or III-11C (274 nM), and incubated in at 37°C, 5% CO_2 for 1 hr. Subsequently, MEFs were rinsed once in warm 1X PBS and fixed

using pre-warmed 4% PFA for 20 min. After fixation, wells were rinsed three times, 5 min each with Stain Buffer (cat # 554656 BD Pharmingen), blocked for 30 min at room using 5% Donkey serum prepared in Stain Buffer, and incubated with the monoclonal anti-Fn1 (Abcam, cat # 199056) overnight at 4° C. Cell were then rinsed with Stain Buffer three times, 10 min each, and incubated with anti-rabbit antibodies conjugated with Alexa-647 for 1 hour at rt. Cell were then rinsed again with Stain Buffer three times, 10 min each, and stored at 4° C in 1X PBS for imaging later.

Hydrogels

Methacrylated Alginate Synthesis: Methacrylated alginate (MeAlg) was synthesized according to a previously established protocol (57). In brief, alginic acid sodium salt from brown algae (Sigma-Aldrich, USA) (3% w/v) was fully dissolved in Dulbecco's phosphate buffered saline (dPBS, Sigma-Aldrich, USA). Then, methacrylic anhydride (Sigma-Aldrich, USA) (8% v/v) was added drop-wise to the alginate solution and stirred for 12 h at 4°C, using 2M NaOH (Sigma-Aldrich, USA) to ensure that the pH remained between 8 and 9 for the duration of the reaction. The resulting solution was passed through filter paper (GE Whatman) and poured into Spectra/Por dialysis membrane with a 6–8 kDa molecular weight cutoff (Fischer Scientific) and kept in DIW under stirring for 7 days to eliminate the unreacted MA and salts. Dialyzed solution was then freeze-dried for 4 days to obtain MeAlg foam.

Fabrication of the Hydrogel Substrates: MeAlg substrates were fabricated using a previously established protocol (58). Briefly, petri dishes with glass bottoms were treated with UV/ozone (UVO) for 30 minutes, immediately followed by a coating of 3-(trimethoxysilyl)propyl methacrylate (TMS) (Sigma-Aldrich, USA) to methacrylate the glass surfaces (59). The dishes were left in a desiccator overnight. The hydrogels were fabricated using Michael-type addition polymerization. First, 2-hydroxy-4'-(2-hydroxyethoxy)-2-methylpropiophenone (I2959) (Sigma-

Aldrich, USA), a photoinitiatior (0.5% w/v) was completely dissolved in Dulbecco's PBS (dPBS), followed by the lyophilized MeAlg (3% w/v) synthesized previously. This was kept at room temperature until a clear solution was achieved. Crosslinking occurs with the introduction of DL-Dithiothreitol (DTT) (Sigma-Aldrich, USA) to the solution, along with 0.2M triethanolamine (Sigma-Aldrich, USA) at pH 10. To form 3kPa and 12 kPa gels, 20% and 30% (w/v) DTT are used, respectively. To promote cell adhesion, GRGDSPC peptide (1% w/v) (Genscript) was added to the solution. After all contents were thoroughly mixed, 5µL of MeAlg solution was pipetted onto the surface of the dish before being covered with a glass coverslip in order to create gels less than 30µm thick. These were left at room temperature for an hour to crosslink before being submerged in dPBS to remove the coverslip.

Atomic Force Microscopy: For stiffness measurements, hydrogel samples were submerged in dPBS and placed in a Dimension Icon AFM with ScanAsyst (Bruker). Using the PeakForce-QNM mode, hydrogel samples were indented using an MLCT-Bio probe tip with pyramidal geometry (Bruker, CA) and a nominal spring constant of 0.03 N/m, checked by thermal calibration.

Treatment of cells with Deoxycholate (DOC)

10^4 $Fn1^{mEGFP/+}$ MEFs were plated for 48 hrs in 8-well glass bottom Ibidi dishes in complete medium and incubated at 37° C and 5% CO_2. Two hours before imaging SiR-actin was added at 1 μM final concentration. SiR-actin contains a far-red dye, silicon rhodamine, conjugated to jasplakinolide that labels F-actin in live and fixed cells (60). Just before imaging, complete medium was replaced by 150 μl imaging medium containing 33 μg/ml of Hoechst 33342. Positions were marked in each well and live imaging was initiated at 37°C and 5 % CO_2 humidified chamber. After 15 min, 150 μl 4% DOC solution prepared in imaging medium containing 33 μg/ml Hoechst was added to the experimental well (final pH 8.01) and 150 μl

imaging medium containing 33 μg/ml Hoechst but without DOC was added to the control well. Cells were imaged at 50 sec intervals until F-actin and DNA disappeared (see Movie 4). The medium was then removed, cells were rinsed for 1 min with 1X PBS pre-warmed to 37°C, fixed with 4% PFA pre-warmed to 37°C, and stained to detect Fn1, as described below.

Immunofluorescence staining of permeabilized cells

MEFs were grown either on #1.5 round glass coverslips in 24-well dishes or in 8-well glass Ibidi dishes depending on the experiment for the times indicated in figure legends. MEFs were then rinsed with 1X PBS (warmed to 37^0 C) for 5 min, fixed with freshly thawed 4% PFA pre-warmed to 37^0 C for 20 min, and washed three times with 1X PBS (warmed to 37^0 C) with mild shaking. All subsequent washing steps were done with shaking. For permeabilization, cells were washed once in 1X PBS containing 0.1% Triton- X 100 (PBST). Blocking was done for 30 min in 5% Donkey serum prepared in PBST (blocking solution). After blocking, cells were incubated in primary antibodies were diluted in blocking solution overnight at 4^0 C, as specified in the table above. This was followed by 3 washes in PBST for 10 min each. Cells were then incubated with secondary antibodies diluted in PBST for 60 min at rt. Finally, cells were washed three times with PBST for 10 min each. DAPI (1:300) was added to the second wash. Cells were mounted using Vectashield.

Imaging

Fixed samples on coverslips and 8-well Ibidi dishes were imaged using Nikon A1-HD25 inverted confocal microscope with the DUG 4-Channel Detector and 2 GaAsP, 2 high-sensitivity PMTs, and a motorized XYZ stage with Nikon's Perfect Focus 4 system. Plan Fluor 40x Oil (numerical aperture 1.3, cat # MRH01401) was used for live imaging, and CFI

Apochromat TIRF 100xC Oil objective with numerical aperture 1.49 (cat # MRD01905) was used with the enhanced resolution protocol, TIRF, and STORM.

Confocal Settings

Confocal images of fixed samples were recorded using Nikon A1-HD25 inverted confocal microscope equipped with CFI Apochromat TIRF 100xC Oil objective with the pinhole set to 0.8 Airy units, and imaged through 2 – 4 microns with step size of 0.125 μm - 0.15 μm at a sampling of 40 nm per pixel. Crop function was used to reduce imaging time and sample bleaching. Deconvolution was done using Nikon 3D deconvolution software (v5.11.01). Airyscan imaging was performed using Zeiss LSM 880 fitted with a 32 array AiryScan GaAsP-PMT detector and the Plan Apochromat 63X Oil (NA 1.4) objective. Deconvolution and pixel reassignment were done using Zeiss LSM software.

Live imaging

Ibidi 8-well glass-bottom slides or MatTek glass bottom dishes were placed into humidified Tokai Hit stage-top incubator maintained at 37° C and a 5% CO_2 atmosphere. mEGFP was excited using 488 nm laser at 1% power and pinhole set to 1 Airy unit. An optical zoom of 2 and Z step size of 0.5 μm were used, and stack size was set to 10-15 microns allowing to image the entire cell. For overnight movies, each position was filmed every 1.5 min – 4 min, as noted in Movie legends, for the DOC assay, imaging was performed at 54 sec intervals.

Movies

Movies in the mp4 format were generated using Imaris 9.5.1 (Bitplane), titles and arrows were added using Adobe Premiere Elements Editor 2020.

570 **TIRF imaging**

571 TIRF microscopy was performed using Nikon A1-HD25 inverted confocal microscope equipped
572 with 4 laser lines of 100mW per line at 405, 488, and 561nm and 125mW at 640nm, and
573 motorized TIRF illumination. CFI Apochromat TIRF 100xC Oil objective and EMCCD camera
574 were used. Before imaging lasers were aligned and the critical angle of incidence for imaging
575 was determined by the software. The exposure time was 20 ms and readout speed was set at
576 10 MHz.

577

578 **STORM imaging**

579 Following IF staining, primary antibodies were detected using secondary antibodies coupled
580 with Alexa-647 fluorescent dye. Samples were washed and stored in PBS at 4^{o}C. Prior to
581 imaging, freshly prepared STORM buffer was added and the chamber was immediately sealed
582 using parafilm. STORM was performed using Nikon A1-HD25 Ti2E microscope equipped with
583 motorized TIRF illumination, 125mW 640 nm solid-state laser, Perfect Focus, and a
584 100x/1.49NA objective. Images were acquired at the critical angle of incidence and recorded
585 using a 512 x 512 EMCCD camera (Princeton Instruments). Calibration, drift correction, and z-
586 rejection were based on the calibration file obtained by imaging of 100 nm Tetraspeck beads
587 (Life technologies, catalog # T-7279) using the same glass surface and buffer conditions. To
588 drive Alexa-647 into the dark state, samples were pre-bleached by the illumination at 640 nm
589 for 10 seconds at 100 % laser power. Images were acquired for 40,000 frames at 8.4 ms
590 exposure. Blinking events were fitted using the Nikon N-STORM localization software. Images
591 in which the Gaussian distribution of spot sizes was centered at 2 – 5 nm were used for further
592 analyses. Localization events with fewer than 800 or more than 50000 photons were filtered
593 out to remove blinking evens that were either too faint or too bright. In addition, blinking events
594 were filtered out if they occurred in more than 3 consecutive periods or where outside the z-

range determined by the calibration using 100 nm Tetraspeck beads. Images in which z-rejection was below 50% were used for the analyses.

Analysis of the number of molecules within non-fibrillar and fibrillar Fn1 nanodomains The free-hand ROI tool in the STORM window (Nikon Elements AR Software v5.11.01) was used to draw ROI around nanodomains in fibrils or non-fibrillar nanodomains in a fibril to get a count of molecule numbers. Fn1 nanodomains were analyzed in 5 random regions from 3 independently acquired images (a total of 15 fields) for each sample/antibody type. To determine the molecule number in Fn1 nanodomains within fibrils, we analyzed more than 20 fibrils per antibody, from 3 or more independently acquired images. All the counts were plotted in Prism 8.2.1 (GraphPad Software, USA), and compared using either one-way ANOVA test with Tukey's correction or Kruskal-Wallis test with Dunn's correction for multiple testing.

Analysis of distance between fluorescence Fn1 nanodomains in fibrils Distances between nanodomains were quantified by measuring the distance between the centers of nanodomain within fibrils using Nikon image analysis software and by Fiji peak analysis plugin, which was done in the following manner: In order to quantify distance between nanodomains in a fibril, a snapshot of the STORM window was generated. Rectangular ROI box was drawn around a fibril and plot profiles were generated. We analyzed more than 20 thin fibrils from 3 or more independently acquired images for each antibody type. Plot profiles were analyzed using Find Peak function in the BAR module of Fiji (Tiago Ferreira et al., (2016) 10.5281/zenodo.28838). Default settings were used to generate lists of maxima and minima for each plot. Lists were extracted to Microsoft Excel and distances between peak maxima were computed. Distances measured manually and automatically were comparable and all were plotted using Prism 8.2.1. See **Supplemental Figure 5a** for the automatic peak finding workflow.

Analysis of distance between non-fibrillar nanodomains In order to quantify distance between non-fibrillar nanodomains in an image, a snapshot of the STORM window was generated. Rectangular ROI box used for analysis of distance between density peaks in a fibril was reloaded and positioned to capture as many non-fibrillar nanodomains as possible in a rectangle. More than 5 regions from 3 or more independently acquired images were analyzed for $Fn1^{mEGFP/+}$ MEFs immunostained with a cocktail of four antibodies, anti-N-terminal Fn1 antibody, monoclonal anti-tFn1, polyclonal anti-tFn1, and anti-GFP antibodies. Plot profiles were analyzed using Find Peak function in the BAR module of Fiji ((Tiago Ferreira et al., (2016) 10.5281/zenodo.28838). Default settings were used to generate lists of maxima and minima for each plot. Lists were extracted to Microsoft Excel and distances between peak maxima were computed. Distances were plotted using Prism 8.2.1. See **Supplemental Figure 5B** for the workflow.

Analysis of area and diameter of non-fibrillar and fibrillar nanodomains Snapshots of 5 regions were generated from 3 independently acquired images and saved as .png files with scale bars. Images were converted to 8-bit files and thresholded in Fiji. “Analyze particle” function was used to extract the area for all nanodomains in the image. These values were copied into an excel file where they were sorted from largest to smallest. Areas smaller than 10^{-4} μm^2 (~11.9 nm in diameter) were excluded from the analyses (see **Supplemental Figure 6A-C**). There were no statistical differences between non-fibrillar nanodomain areas of untreated, FUD- or 11-IIIC treated cells without filtering (**Supplemental Figure 6D-E**). The values for nanodomain diameters were extracted from the area measurements and confirmed manually for a smaller sample, by measuring nanodomain diameters using the Nikon software.

Figure Legends

Figure 1. Beaded architecture of Fn1 fibrils in embryonic ECM. Wild-type E9.5 mouse embryos were fixed and stained with the monoclonal antibody to Fn1 (white) and DAPI, and imaged using 100x oil objective, N.A. 1.49, pinhole 0.8, and sampling rate of 40 nm/pixel. **A – A1.** Sagittal optical section through the first pharyngeal arch and **b.** the cardiac jelly, an ECM-rich region between the myocardial and endocardial layers of the outflow tract of the heart. Large arrowheads in **A – A1** point to the ECM at the ectoderm-mesenchyme boundary of the 1st pharyngeal arch. The box in **(A)** is expanded in **A1** to show the beaded Fn1 microarchitecture. Arrow in **A1** points to Fn1 fibril within the arch mesenchyme; **B.** Beaded architecture of Fn1 fibrils in cardiac jelly, e.g., arrow. **C.** Intensity profile plot of a Fn1 fibril shows a regularly-undulating profile, with peaks corresponding with Fn1 "beads"; a.u. arbitrary units.

Figure 2. Integrin α5β1 and Fn1 co-localize in beaded adhesions. Wild-type MEFs were plated for 16 hours on glass coverslips, then fixed, stained with antibodies to Fn1 and integrin α5 (Itga5), and imaged at the critical angle of incidence using 100x oil objective, NA 1.49. **A – A2** cell periphery. Arrows in **A – A2** point to examples of non-fibrillar Fn1 adhesions ("beads") at cell periphery. **B - B2** medial portion of a cell containing beaded fibrillar adhesions (arrows). Note that both Itga5 and Fn1 stainings are beaded. Magnifications in all panels are the same.

Figure 3. Beaded architecture of Fn1 fibrils is present in fibrils between cells and is retained in the absence of cell contact. A – B. Fn1 secreted by wild-type MEFs and deposited **A)** on glass or **B)** between cells. **C.** Fn1 fibrils between endothelial cells. Boxes in **A– C** are magnified in **A1-C1**. Arrows point to fibrils left behind on substrata (**A1**) or between cells (**B1-C1**). **d.** Fn1$^{Neon\ Green}$ MEFs were treated with 2% DOC pH 8 until cells were dissolved

(see Movie 3). Following DOC treatment, Fn1 was imaged using 100x oil objective, NA 1.49, pinhole size 0.8 Airy units, and sampling resolution of 40 nm/pixel in x,y. Note beaded architecture (arrows).

Figure 4. Fn1 fibrils are composed linear arrays of Fn1 nanodomains. $Fn1^{mEGFP/+}$ MEFs were plated on glass for 16 hrs, then fixed and stained with antibodies to GFP followed by secondary antibodies conjugated to Alexa-647. **A.** Native GFP fluorescence imaged by TIRF using 100x objective NA 1.49. Arrow in **A** points to a thin, beaded Fn1 fibril resolved by STORM in **B1, B1'** and **B2. B.** The entire field of view in **A** is imaged by STORM detecting Alexa-Fluor 647-conjugated antibody (see Methods). The box in **B** is expanded in **B1**. The box in **B1** is expanded in **B2**. The arrow in **B1** points to the same region as the arrow in **A**. Arrows in **B2** point to Fn1 nanodomains; arrowheads point to Fn1 localizations between the nanodomains, notched arrowheads point to Fn1 nanodomains that are not in fibrils and wide arrows point to Fn1-free areas between the nanodomains in the fibril marked by the arrow in **A**. **A, B, B1, B1'** and **B2** are in x-y planes; **B2'** shows the nanodomains in **B2** in the x-z plane. Images in **B1'** and **B2'** are depth-coded according to the scale in **B1'**. See Movie 4 for 3D rotation of the fibril underlined in **B1'** around the x-axis.

Figure 5. Fn1 fibrils are composed of nanodomains containing multiple Fn1 dimers. Wild-type or $Fn1^{mEGFP/+}$ MEFs were plated on glass for 16 hrs, fixed and stained with different antibodies to Fn1 followed by Alexa 647-conjugated secondary antibodies. Columns showing cells treated with DOC prior to fixation are marked. Cells were imaged using STORM**. A.** zoom-out views to show the overall appearance of Fn1 fibrils. **B-E.** Successive magnifications of fibrils shown in (**A**). Arrows in **D** point to nanodomains magnified in **E;** arrowheads in **D-E** point to Fn1 molecules between nanodomains, wide open arrows point to Fn1-free zones between nanodomains in a fibril. **F.** distances between nanodomains within fibrils or non-

698 fibrillar (NF) nanodomains, **** $p<10^{-4}$, Kruskal-Wallis test, with Dunn's correction for multiple
699 testing. Inset in **F** is a plot profile of the fibril marked by the box in the column **6D** showing
700 regularly-spaced peaks of intensity. DOC-treated samples are marked. 4-antibody cocktail
701 contains four antibodies as in **Model 1**. **G.** Diameter of nanodomains in fibrils. **H.** number of
702 Fn1 localizations per nanodomain in fibrils. **Model 1**. Two Fn1 dimers in a fibril. Depiction of
703 antibody coverage of Fn1 fibrils if dimers were oriented in end-to-end fashion with alternating
704 N- and C-termini. **Model 2.** Our data show that Fn1 fibrils consist of a linear array of
705 nanodomains (black arrows) containing multiple Fn1 dimers (Fn1 dimers are depicted as balls
706 and color-coded according to the antibody scheme in **Model 1**. Arrowheads point to Fn1 and
707 open arrows point to Fn1-free areas between nanodomains.
708
709 **Figure 6. The N-terminal Fn1 assembly domain regulates the organization of Fn1**
710 **nanodomains into linear fibrillar arrays**. $Fn1^{mEGFP/+}$ MEFs were plated on glass and were
711 either left untreated, or were incubated with the control 11-IIIC peptide, or the FUD peptide for
712 16 hrs. Cell were then fixed and stained with the monoclonal antibody to Fn1 followed by Alexa
713 647-conjugated secondary antibodies. Cells were imaged at the critical angle of incidence by
714 STORM. **A – A2**. Untreated, unpermeabilized cells. **B – B2.** Cells incubated with controls 11-
715 IIIC peptide. **C – C1, C1-1** FUD-treated, unpermeabilized cells. Boxes marked 1 in **A-B** were
716 expanded in **A1-B1**. Boxes marked 2 in **A-B**, were expanded in **A2 – B2**. The box in **C** is
717 expanded in **C1** and **C1-1**. Arrows in **A1-B1** point to Fn1 nanodomains (NDs) in fibrils. Arrows
718 in **C1** points to non-fibrillar nanodomains expanded in **C1-1**; **D.** Quantification of the number of
719 Fn1 localizations in NDs in fibrils and in non-fibrillar NDs after various conditions. Red lines
720 mark medians. Differences are not statistically significant, Kruskal-Wallis test with Dunn's
721 correction for multiple testing. **E.** Model of fibril formation: Fn1 dimers assemble into small
722 nanodomains containing integrin $\alpha5\beta1$ at cell periphery, move rearward with actin flow, and

become organized into linear arrays of nanodomains. Joining of the additional Fn1 nanodomains to these arrays leads to the generation of longer fibrils as the assembly moves toward the cell center. FUD does not interfere with the formation of Fn1 nanodomains. But instead, it blocks the organization of Fn1 nanodomains into linear arrays.

Legends for Movies

Movie 1. Rotational views through the Fn1+ ECM in the cardiac jelly. Whole E9.5 embryo was stained using rabbit monoclonal anti-Fn1 antibody and imaged using 100x objective, N.A. 1.49, with the pinhole set at 0.8 Airy units, and sampling of 40 nm per pixel in x, y. The movie shows 3D reconstruction through 3.4 μm of tissue sampled every 0.121 μm in z. Fn1 is in white, DAPI is in blue. Arrows point to examples of beaded Fn1 fibrils.

Movie 2. Fn1 fibrillogenesis imaged by TIRF microscopy. $Fn1^{mEGFP}$ MEFs were transiently transfected with mCardinal-lifeact, plated on gelatin-coated glass cover slips, and imaged 48 hours later. Filming was done every 2 min for 30 min using TIRF and 100x objective, N.A. 1.49. The first set shows Fn1-mEGFP channel. Yellow arrows point to centripetally-moving Fn1 nanodomains that appear to be organizing into an elongating linear fibril. The second set is an overlay between Fn1-mEGFP and mCardinal-lifeact.

Movie 3. 2% DOC dissolved cytoplasm and nucleus in under 13 min leaving Fn1 fibrils. MEFs expressing Fn1-mEGFP were plated on glass-bottom slides and labeled with SiRActin (magenta) to visualize F-actin and Hoechst (blue) to visualize DNA. Time lapse was recorded every 54 sec immediately following the addition of DOC solution, pH 8.01, to live cells. The addition of 2% DOC dissolves actin cytoskeleton and nuclei, and leaves Fn1 ECM fibrils

747 (green). Fn1 fibrils collapse following the dissolution of the actin cytoskeleton due to the loss of
748 tension.
749
750 **Movie 4. 3D-rendering of STORM data.** Fn1 fibril underlined in Fig. 4b1 is rotated around the
751 x-axis to show the arrangement of Fn1 localizations in 3D. The movie starts in x-y plane.
752 Yellow arrows point at Fn1 nanodomains in the fibrils. Red arrows point to the space between
753 the nanodomains.
754
755 **Movie 5. Cells incubated with 11-IIIC, show robust fibrillogenesis.** $Fn1^{mEGFP}$ MEFs were
756 plated on glass in 8-well Ibidi chambers for 4 hours, Medium containing 11-IIIC control peptide
757 was then added and cells were filmed every 90 sec for about 15 hours, as described in
758 Methods. The movie begins approximately 30 min after the 11-IIIC-containing medium was
759 added, the time it takes to set up time-laps recording. Arrows point to cell periphery and
760 examples of centripetally moving Fn1 fibrils.
761
762 **Movie 6. FUD interferes with linking centripetally moving Fn1+ nanodomains into fibrils.**
763 $Fn1^{mEGFP}$ MEFs were plated on glass in 8-well Ibidi chambers for 4 hours. Medium containing
764 FUD peptide was then added and cells were filmed every 3 min for about 15 hours, as
765 described in Methods. The movie begins approximately 30 min after the FUD-containing
766 medium was added, the time it takes to set up time-laps recording. Note the dismantling of pre-
767 existing fibrils at the beginning of the movie. Yellow and red arrows point to cell periphery.
768 Note the presence of centripetally moving Fn1-mEGFP “beads” and the scarcity of Fn1 fibrils
769 for the majority of the duration of the movie.
770

References

1. J. E. Schwarzbauer, D. W. DeSimone, Fibronectins, their fibrillogenesis, and in vivo functions. *Cold Spring Harbor perspectives in biology* **3** (2011).

2. T. Rozario, B. Dzamba, G. F. Weber, L. A. Davidson, D. W. DeSimone, The physical state of fibronectin matrix differentially regulates morphogenetic movements in vivo. *Dev Biol* **327**, 386-398 (2009).

3. P. Singh, J. E. Schwarzbauer, Fibronectin matrix assembly is essential for cell condensation during chondrogenesis. *J Cell Sci* **127**, 4420-4428 (2014).

4. H. Y. Chiang, V. A. Korshunov, A. Serour, F. Shi, J. Sottile, Fibronectin is an important regulator of flow-induced vascular remodeling. *Arterioscler Thromb Vasc Biol* **29**, 1074-1079 (2009).

5. X. Zhou *et al.*, Fibronectin fibrillogenesis regulates three-dimensional neovessel formation. *Genes Dev* **22**, 1231-1243 (2008).

6. M. L. Smith *et al.*, Force-induced unfolding of fibronectin in the extracellular matrix of living cells. *PLoS Biol* **5**, e268 (2007).

7. Q. Zhang, W. J. Checovich, D. M. Peters, R. M. Albrecht, D. F. Mosher, Modulation of cell surface fibronectin assembly sites by lysophosphatidic acid. *J Cell Biol* **127**, 1447-1459 (1994).

8. Q. Zhang, M. K. Magnusson, D. F. Mosher, Lysophosphatidic acid and microtubule-destabilizing agents stimulate fibronectin matrix assembly through Rho-dependent actin stress fiber formation and cell contraction. *Mol Biol Cell* **8**, 1415-1425 (1997).

9. C. Zhong *et al.*, Rho-mediated contractility exposes a cryptic site in fibronectin and induces fibronectin matrix assembly. *J Cell Biol* **141**, 539-551 (1998).

10. M. A. Chernousov, A. I. Faerman, M. G. Frid, O. Printseva, V. E. Koteliansky, Monoclonal antibody to fibronectin which inhibits extracellular matrix assembly. *FEBS Lett* **217**, 124-128 (1987).

11. B. Geiger, A. Bershadsky, R. Pankov, K. M. Yamada, Transmembrane crosstalk between the extracellular matrix--cytoskeleton crosstalk. *Nature reviews. Molecular cell biology* **2**, 793-805 (2001).

12. B. Geiger, K. M. Yamada, Molecular architecture and function of matrix adhesions. *Cold Spring Harb Perspect Biol* **3** (2011).

13. E. Zamir *et al.*, Dynamics and segregation of cell-matrix adhesions in cultured fibroblasts. *Nat Cell Biol* **2**, 191-196 (2000).

14. J. Lu *et al.*, Basement Membrane Regulates Fibronectin Organization Using Sliding Focal Adhesions Driven by a Contractile Winch. *Dev Cell* **52**, 631-646 e634 (2020).

15. R. Pankov *et al.*, Integrin dynamics and matrix assembly: tensin-dependent translocation of alpha(5)beta(1) integrins promotes early fibronectin fibrillogenesis. *J Cell Biol* **148**, 1075-1090 (2000).

16. E. Zamir *et al.*, Molecular diversity of cell-matrix adhesions. *J Cell Sci* **112 (Pt 11)**, 1655-1669 (1999).

17. S. M. Fruh, I. Schoen, J. Ries, V. Vogel, Molecular architecture of native fibronectin fibrils. *Nat Commun* **6**, 7275 (2015).

18. B. J. Dzamba, D. M. Peters, Arrangement of cellular fibronectin in noncollagenous fibrils in human fibroblast cultures. *J Cell Sci* **100 (Pt 3)**, 605-612 (1991).

19. Y. Chen, L. Zardi, D. M. Peters, High-resolution cryo-scanning electron microscopy study of the macromolecular structure of fibronectin fibrils. *Scanning* **19**, 349-355 (1997).

20. M. G. Choi, R. O. Hynes, Biosynthesis and processing of fibronectin in NIL.8 hamster cells. *J Biol Chem* **254**, 12050-12055 (1979).

21. P. Singh, C. Carraher, J. E. Schwarzbauer, Assembly of fibronectin extracellular matrix. *Annu Rev Cell Dev Biol* **26**, 397-419 (2010).

22. I. Wierzbicka-Patynowski, Y. Mao, J. E. Schwarzbauer, Analysis of fibronectin matrix assembly. *Current protocols in cell biology / editorial board, Juan S. Bonifacino ... [et al.]* **Chapter 10**, Unit 10 12 (2004).

23. P. J. McKeown-Longo, D. F. Mosher, Binding of plasma fibronectin to cell layers of human skin fibroblasts. *J Cell Biol* **97**, 466-472 (1983).

24. J. H. Peters, R. O. Hynes, Fibronectin isoform distribution in the mouse. I. The alternatively spliced EIIIB, EIIIA, and V segments show widespread codistribution in the developing mouse embryo. *Cell Adhes Commun* **4**, 103-125 (1996).

25. A. Jimenez, K. Friedl, C. Leterrier, About samples, giving examples: Optimized Single Molecule Localization Microscopy. *Methods* **174**, 100-114 (2020).

26. K. Skorstengaard, M. S. Jensen, P. Sahl, T. E. Petersen, S. Magnusson, Complete primary structure of bovine plasma fibronectin. *Eur J Biochem* **161**, 441-453 (1986).

27. M. E. Vega, B. Kastberger, B. Wehrle-Haller, J. E. Schwarzbauer, Stimulation of Fibronectin Matrix Assembly by Lysine Acetylation. *Cells* **9** (2020).

28. S. Rickelt, R. O. Hynes, Antibodies and methods for immunohistochemistry of extracellular matrix proteins. *Matrix Biol* **71-72**, 10-27 (2018).

29. J. E. Schwarzbauer, Identification of the fibronectin sequences required for assembly of a fibrillar matrix. *J Cell Biol* **113**, 1463-1473 (1991).

30. J. L. Sechler *et al.*, A novel fibronectin binding site required for fibronectin fibril growth during matrix assembly. *J Cell Biol* **154**, 1081-1088 (2001).

31. B. R. Tomasini-Johansson *et al.*, A 49-residue peptide from adhesin F1 of Streptococcus pyogenes inhibits fibronectin matrix assembly. *J Biol Chem* **276**, 23430-23439 (2001).

32. A. Morla, Z. Zhang, E. Ruoslahti, Superfibronectin is a functionally distinct form of fibronectin. *Nature* **367**, 193-196 (1994).

33. J. L. Sechler, Y. Takada, J. E. Schwarzbauer, Altered rate of fibronectin matrix assembly by deletion of the first type III repeats. *J Cell Biol* **134**, 573-583 (1996).

34. M. S. Filla, K. D. Dimeo, T. Tong, D. M. Peters, Disruption of fibronectin matrix affects type IV collagen, fibrillin and laminin deposition into extracellular matrix of human trabecular meshwork (HTM) cells. *Exp Eye Res* **165**, 7-19 (2017).

35. L. M. Maurer *et al.*, Extended binding site on fibronectin for the functional upstream domain of protein F1 of Streptococcus pyogenes. *J Biol Chem* **285**, 41087-41099 (2010).

36. J. Sottile, J. Chandler, Fibronectin matrix turnover occurs through a caveolin-1-dependent process. *Mol Biol Cell* **16**, 757-768 (2005).

37. R. Y. Tsien, The green fluorescent protein. *Annual review of biochemistry* **67**, 509-544 (1998).

38. C. K. Choi *et al.*, Actin and alpha-actinin orchestrate the assembly and maturation of nascent adhesions in a myosin II motor-independent manner. *Nat Cell Biol* **10**, 1039-1050 (2008).

39. C. H. Damsky, K. A. Knudsen, D. Bradley, C. A. Buck, A. F. Horwitz, Distribution of the cell substratum attachment (CSAT) antigen on myogenic and fibroblastic cells in culture. *J Cell Biol* **100**, 1528-1539 (1985).

40. F. Zhang, S. Saha, A. Kashina, Arginylation-dependent regulation of a proteolytic product of talin is essential for cell-cell adhesion. *J Cell Biol* **197**, 819-836 (2012).

41. D. M. Peters, L. M. Portz, J. Fullenwider, D. F. Mosher, Co-assembly of plasma and cellular fibronectins into fibrils in human fibroblast cultures. *J Cell Biol* **111**, 249-256 (1990).

42. L. M. Maurer, W. Ma, D. F. Mosher, Dynamic structure of plasma fibronectin. *Crit Rev Biochem Mol Biol* **51**, 213-227 (2015).

43. W. Ma, H. Ma, D. F. Mosher, On-Off Kinetics of Engagement of FNI Modules of Soluble Fibronectin by beta-Strand Addition. *PLoS One* **10**, e0124941 (2015).

44. Y. Arai *et al.*, Tying a molecular knot with optical tweezers. *Nature* **399**, 446-448 (1999).

45. A. M. Saitta, P. D. Soper, E. Wasserman, M. L. Klein, Influence of a knot on the strength of a polymer strand. *Nature* **399**, 46-48 (1999).

46. T. Ohashi, D. P. Kiehart, H. P. Erickson, Dynamics and elasticity of the fibronectin matrix in living cell culture visualized by fibronectin-green fluorescent protein. *Proc Natl Acad Sci U S A* **96**, 2153-2158 (1999).

877 47. E. S. Wijelath *et al.*, Novel Vascular Endothelial Growth Factor Binding Domains of
878 Fibronectin Enhance Vascular Endothelial Growth Factor Biological Activity. *Circulation*
879 *research* **91**, 25-31 (2002).

880 48. M. M. Martino, J. A. Hubbell, The 12th-14th type III repeats of fibronectin function as a
881 highly promiscuous growth factor-binding domain. *FASEB J* **24**, 4711-4721 (2010).

882 49. J. T. Saunders, J. E. Schwarzbauer, Fibronectin matrix as a scaffold for procollagen
883 proteinase binding and collagen processing. *Mol Biol Cell* **30**, 2218-2226 (2019).

884 50. R. O. Hynes, The extracellular matrix: not just pretty fibrils. *Science* **326**, 1216-1219
885 (2009).

886 51. S. Snitkovsky, J. A. Young, Cell-specific viral targeting mediated by a soluble retroviral
887 receptor-ligand fusion protein. *Proc Natl Acad Sci U S A* **95**, 7063-7068 (1998).

888 52. F. A. Ran *et al.*, Genome engineering using the CRISPR-Cas9 system. *Nat Protoc* **8**,
889 2281-2308 (2013).

890 53. V. Pliatsika, I. Rigoutsos, "Off-Spotter": very fast and exhaustive enumeration of
891 genomic lookalikes for designing CRISPR/Cas guide RNAs. *Biol Direct* **10**, 4 (2015).

892 54. A. R. Perez *et al.*, GuideScan software for improved single and paired CRISPR guide
893 RNA design. *Nat Biotechnol* **35**, 347-349 (2017).

894 55. R. Behringer, M. Gertsenstein, K. Vintersten, A. Nagy, *Manipulating the Mouse Embryo:*
895 *A Laboratory Manual* (Cold Spring Harbor Laboratory Press, New York, ed. 4th, 2014), pp.
896 814.

897 56. G. T. Dempsey, J. C. Vaughan, K. H. Chen, M. Bates, X. Zhuang, Evaluation of
898 fluorophores for optimal performance in localization-based super-resolution imaging. *Nat*
899 *Methods* **8**, 1027-1036 (2011).

900 57. S. Khetan *et al.*, Degradation-mediated cellular traction directs stem cell fate in
901 covalently crosslinked three-dimensional hydrogels. *Nature Materials* **12**, 458-465 (2013).

902 58. M. Guvendiren, J. A. Burdick, Stiffening hydrogels to probe short- and long-term cellular
903 responses to dynamic mechanics. *Nat Commun* **3**, 792 (2012).

904 59. M. Guvendiren, S. Yang, J. A. Burdick, Swelling-Induced Surface Patterns in Hydrogels
905 with Gradient Crosslinking Density. *Advanced Functional Materials* **19**, 3038-3045 (2009).

906 60. G. Lukinavicius *et al.*, Fluorogenic probes for live-cell imaging of the cytoskeleton. *Nat*
907 *Methods* **11**, 731-733 (2014).
908

Table 1

Distance between Fn1-containing nanodomains in fibrils and in non-fibrillar nanodomains

Cell type / antibody	Median, nm	Interquartile range, nm	n
Distance between nanodomains in fibrils, nm			
Wild-type MEFs α III_{1-6} Fn1 (R184 ab)	148.5	108 – 187	202
Wild-type MEFs monoclonal α Fn1	140	105 – 166	134
Wild-type MEFs polyclonal 297.1	145	107 – 193	159
DOC-treated Wild-type MEFs monoclonal α Fn1	123	83 – 160	148
$Fn1^{mEGFP/+}$ monoclonal α Fn1	124	99 – 166	120
$Fn1^{mEGFP/+}$ α GFP	115	89 – 155	142
$Fn1^{mEGFP/+}$ 4-antibody cocktail	114	82 - 156	106
Distance between non-fibrillar nanodomains, nm			
Non-fibrillar nanodomains $Fn1^{mEGFP/+}$ 4-antibody cocktail	329	260 – 410	132

Table 2
Area of Fn1 nanodomains

Cell type / antibody	Median 10^{-3} μm^2	Interquartile range, 10^{-3} μm^2	n
Area of nanodomains in fibrils, 10^{-3} μm^2			
Wild-type MEFs α III_{1-6} Fn1 (R184 ab)	5	3 – 7	60
Wild-type MEFs monoclonal α Fn1	5	3 – 6	66
Wild-type MEFs polyclonal 297.1	4	3 – 6	62
$Fn1^{mEGFP/+}$ monoclonal α Fn1	3	2 – 5	65
$Fn1^{mEGFP/+}$ α GFP	4	2 – 6	63
$Fn1^{mEGFP/+}$ 4-antibody cocktail	4	3 – 6	62
Area of non-fibrillar nanodomains, 10^{-3} μm^2			
Untreated $Fn1^{mEGFP/+}$ monoclonal α Fn1 16 hr plating	4.3	3– 6	127
11-IIIC treated $Fn1^{mEGFP/+}$ monoclonal α Fn1 16 hr plating	3	2.4 - 4	93
FUD-treated $Fn1^{mEGFP/+}$ monoclonal α Fn1 16 hr plating	4	3 – 6	666

Table 3
Number of localizations per Fn1 nanodomain

Cell type / antibody	Median	Interquartile range	n
Number of Fn1 localizations per nanodomain within fibrils			
Wild-type MEFs α III_{1-6} Fn1 (R184 ab)	72	46.5 - 112	345
Wild-type MEFs monoclonal α Fn1	60	43 – 81	271
Wild-type MEFs polyclonal 297.1	66	42 – 106.5	381
DOC-treated Wild-type MEFs monoclonal α Fn1	72	46 – 113	112
$Fn1^{mEGFP/+}$ monoclonal α Fn1	63	45.25 – 114	216
$Fn1^{mEGFP/+}$ α GFP	61	39 – 92	351
$Fn1^{mEGFP/+}$ 4-antibody cocktail	73	50 – 103	314
Number of Fn1 localizations per non-fibrillar nanodomain			
$Fn1^{mEGFP/+}$ 4-antibody cocktail	58.5	39 – 95	62
Untreated $Fn1^{mEGFP/+}$ monoclonal α Fn1 Unpermeabilized cells	45	33 – 68	127
11-IIIC treated $Fn1^{mEGFP/+}$ monoclonal α Fn1	46	29 – 68.5	93
FUD-treated $Fn1^{mEGFP/+}$ monoclonal α Fn1 Unpermeabilized cells	54.5	37 – 92	102

Figure 1

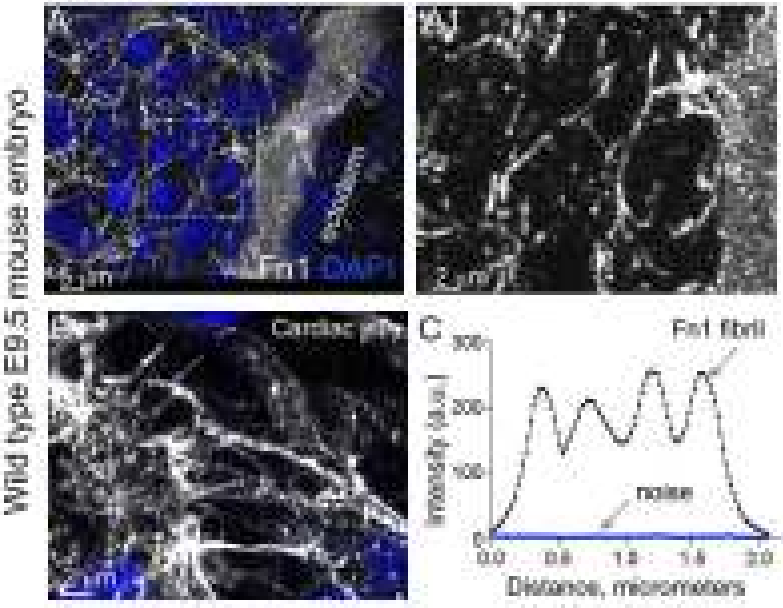

Figure 1. Beaded architecture of Fn1 fibrils in embryonic ECM. Wild-type E9.5 mouse embryos were fixed and stained with the monoclonal antibody to Fn1 (white) and DAPI, and imaged using 100x oil objective, N.A. 1.49, pinhole 0.8, and sampling rate of 40 nm/pixel. **A – A1.** Sagittal optical section through the first pharyngeal arch and **B.** the cardiac jelly, an ECM-rich region between the myocardial and endocardial layers of the outflow tract of the heart. Large arrowheads in **A – A1** point to the ECM at the ectoderm-mesenchyme boundary of the 1st pharyngeal arch. The box in **(A)** is expanded in **A1** to show Fn1 microarchitecture. Arrow in **A1** points to Fn1 fibril within the arch mesenchyme; **B.** Beaded architecture of Fn1 fibrils in cardiac jelly, e.g., arrow. **C.** Intensity profile plot of a Fn1 fibril shows a regularly-undulating profile, with troughs well above the noise; a.u. arbitrary units.

Figure 2

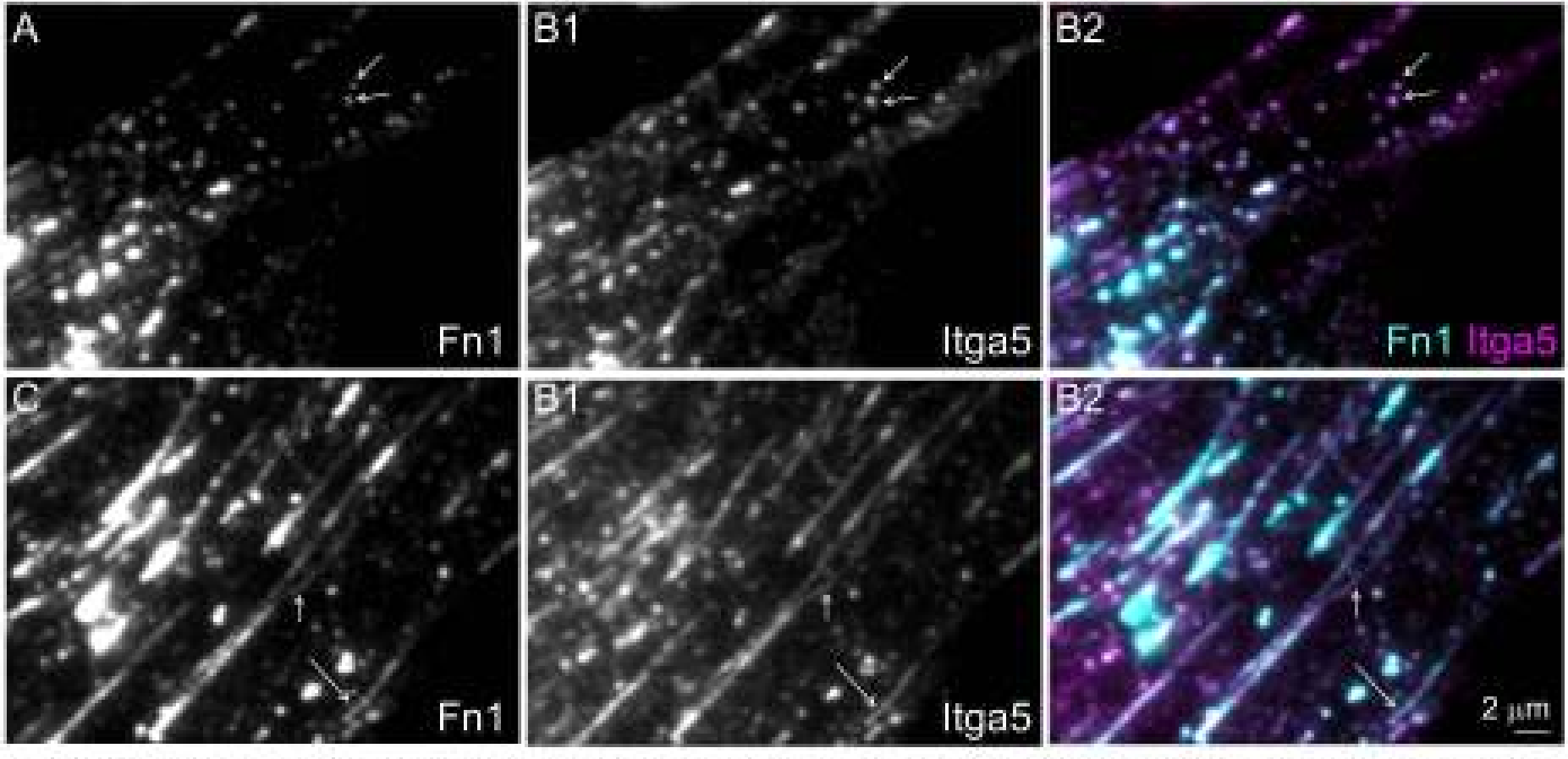

Figure 2. Integrin α5 and Fn1 co-localize in beaded adhesions. Wild-type MEFs were plated for 16 hours on glass coverslips, then fixed, stained with antibodies to Fn1 and integrin α5 (Itga5), and imaged at the critical angle of incidence using 100x oil objective, NA 1.49. **A – A2** cell periphery. Arrows in **A-A2** point at examples of non-fibrillar Fn1 adhesions. **B – B2** medial portion of a cell containing beaded fibrillar adhesions (arrows). Magnifications in all panels are the same.

Figure 3

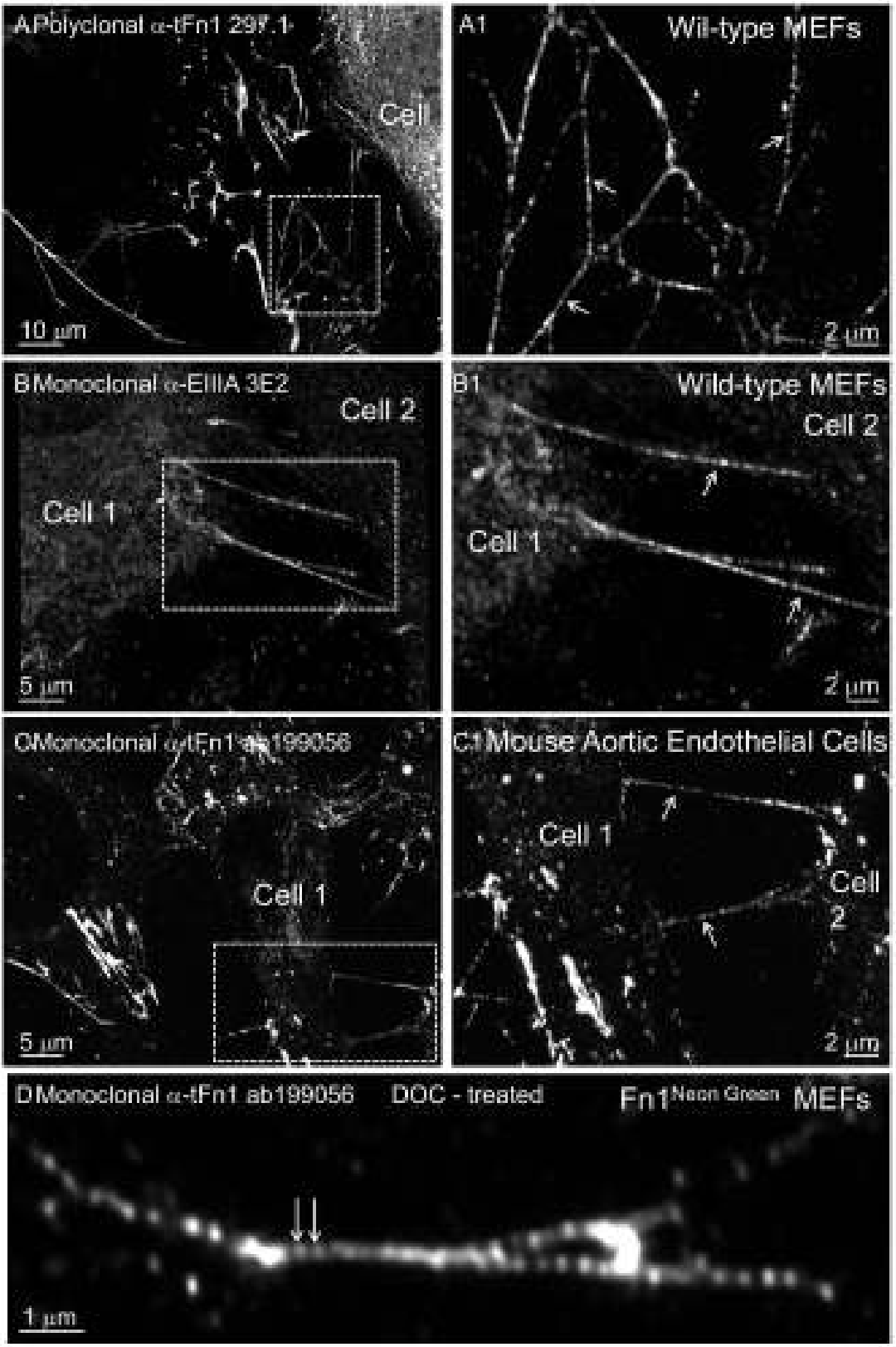

Figure 3. Beaded architecture of Fn1 fibrils is retained in the absence of cell contact. A –B. Fn1 secreted by wild type MEFs and deposited **A)** on glass or **B)** between cells. **C.** Fn1 fibrils between endothelial cells. Boxes in **A – C** are magnified in **A1-C1**. Arrows point to fibrils left behind on substrata (**A1**) or between cells (**B1-C1**). **E.** Fn1 fibril following DOC treatment was imaged using 100x oil objective, NA 1.49, pinhole size 0.8 Airy units, and sampling resolution of 40 nm/pixel in x,y. Note beaded architecture (arrow). Solubilization of cell components is shown in Movie 4.

Figure 4

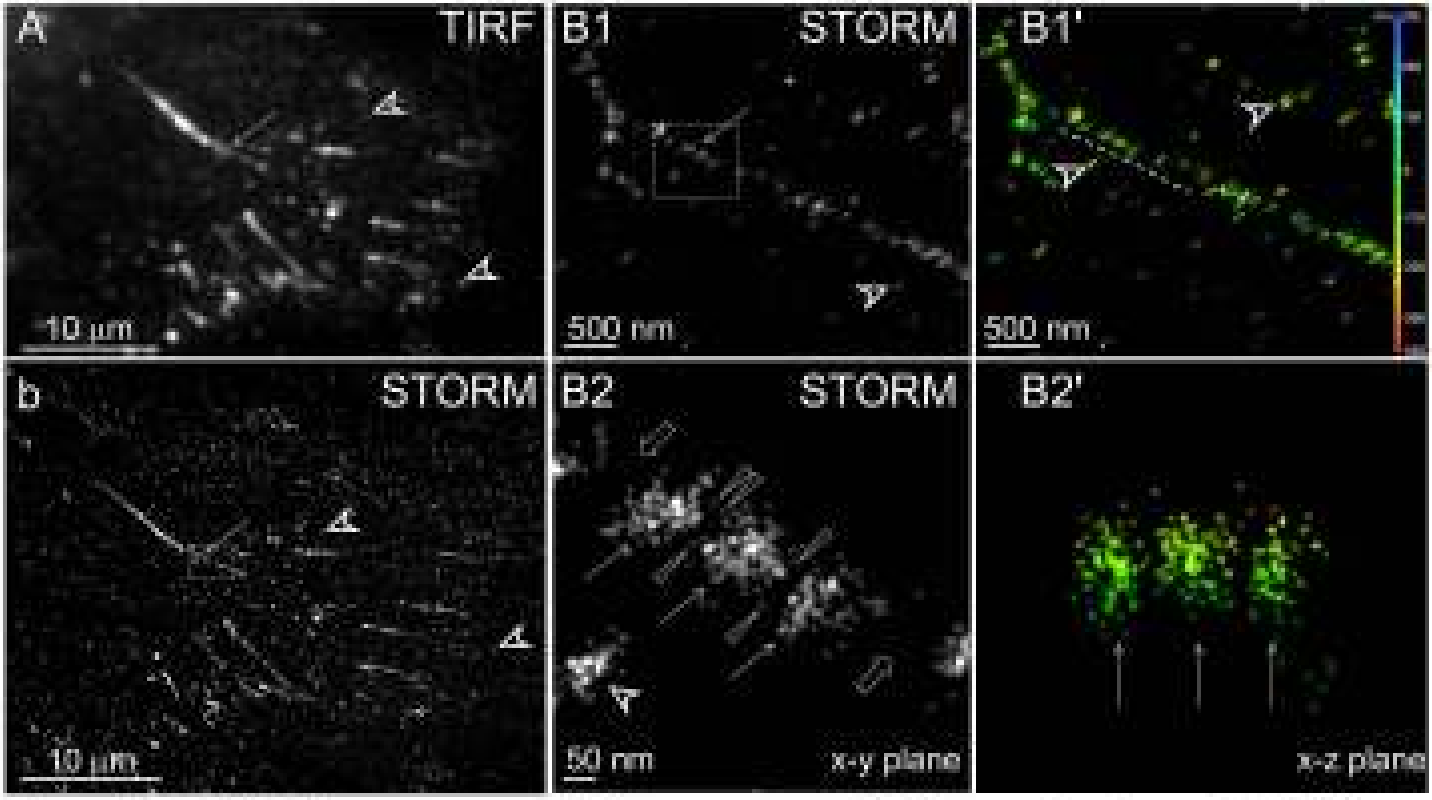

Figure 4. Fn1 fibrils are composed linear arrays of Fn1 nanodomains. $Fn1^{mEGFP/+}$ MEFs were plated on glass for 16 hrs, then fixed and stained with antibodies to GFP followed by secondary antibodies conjugated to Alexa-647. **A.** Native GFP fluorescence imaged by TIRF using 100x objective NA 1.49. Arrow in **a** points to a thin, beaded Fn1 fibril resolved by STORM in **B1** and **B2. B.** The entire field of view in **a** is imaged by STORM detecting Alexa-Fluor 647-conjugated antibody (see Methods). The box in **b** is expanded in **B1**. The box in **B1** is expanded in **B2**. The arrow in **B1** points to the same region as the arrow in **A**. Arrows in **B2** point to Fn1 nanodomains; arrowheads point to Fn1 localizations between the nanodomains, notched arrowheads point to Fn1 nanodomains that are not in fibrils, and wide arrows point to Fn1-free areas between the nanodomains in the fibril marked by the arrow in **A**. **A, B, B1, B1'** and **B2** are in x-y planes; **B2'** is in x-z plane. Images in **B1'** and **B2'** are depth-coded according to the scale in **B1'**. See Movie 4 for 3D rotation of the fibril underlined in **B1'** around the x-axis.

Figure 5

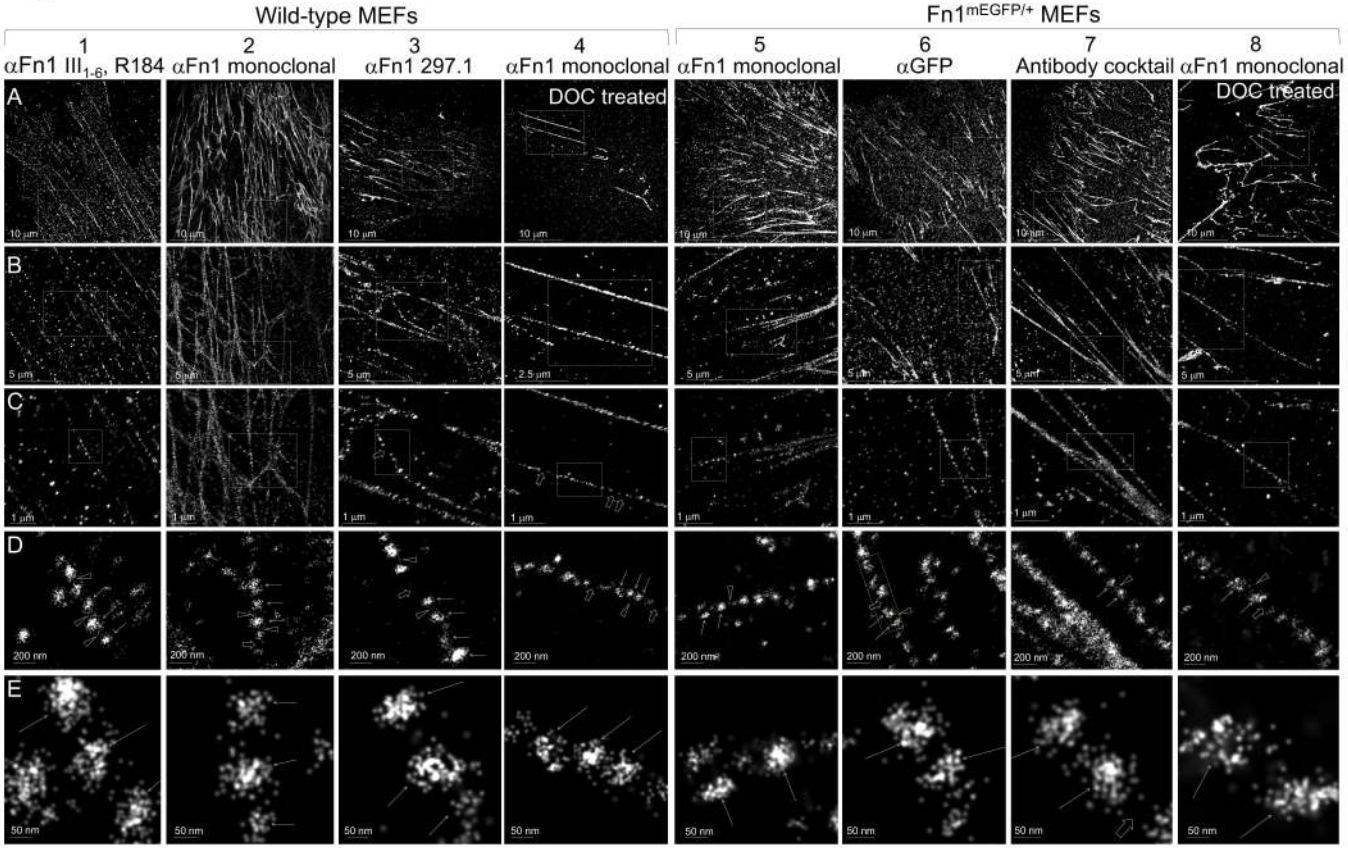

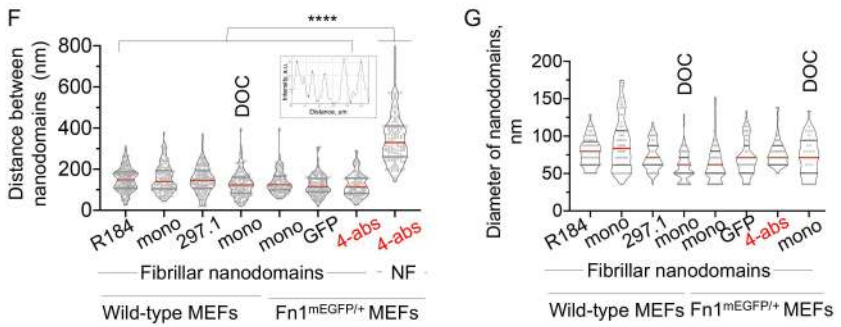

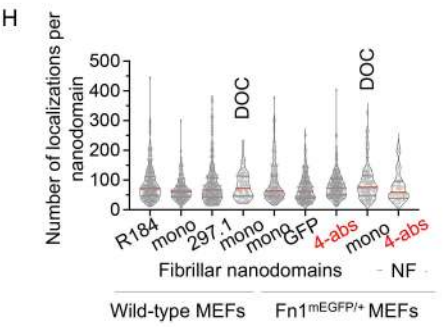

Model 1 Two Fn1 dimers aligned in a periodical end-to-end fashion. If fibrils were composed of periodically aligned dimers, they would be uniformly stained by the antibody cocktail:

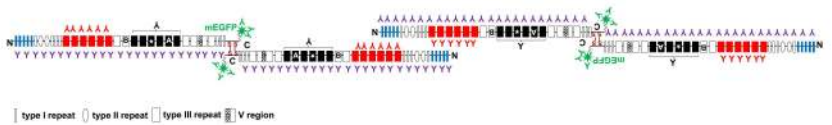

Model 2 Fn1 fibrils form from nanodomains containing multiple Fn1 dimers

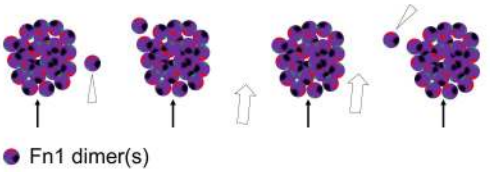

Figure 5. Wild-type or Fn1$^{mEGFP/+}$ MEFs were plated on glass for 16 hrs, fixed and stained with different antibodies to Fn1 followed by Alexa 647-conjugated secondary antibodies. Columns showing cells treated with DOC prior to fixation are marked. Cells were imaged using STORM. **A.** zoom-out views to show the overall appearance of Fn1 fibrils. **B-E.** Successive magnifications of fibrils shown in (**A**). Arrows in **D** point to nanodomains magnified in **E;** arrowheads in **D-E** point to Fn1 molecules between nanodomains, wide open arrows point to Fn1-free zones between nanodomains in a fibril. **F.** distances between nanodomains within fibrils or non-fibrillar (NF) nanodomains, **** $p<10^{-4}$, Kruskal-Wallis test, with Dunn's correction for multiple testing. Inset in **F** is a plot profile of the fibril marked by the box in the column **6D** showing regularly-spaced peaks of intensity. DOC-treated samples are marked. 4-antibody cocktail contains four antibodies as in **Model 1**. **G.** Diameter of nanodomains in fibrils. **H.** number of Fn1 localizations per nanodomain in fibrils. **Model 1**. Two Fn1 dimers in a fibril. Depiction of antibody coverage of Fn1 fibrils if dimers were oriented in end-to-end fashion with alternating N- and C-termini. **Model 2.** Our data show that Fn1 fibrils consist of a linear array of nanodomains (black arrows) containing multiple Fn1 dimers (Fn1 dimers are depicted as balls and color-coded according to the antibody scheme in **Model 1**. Arrowheads point to Fn1 and open arrows point to Fn1-free areas between nanodomains.

Figure 6

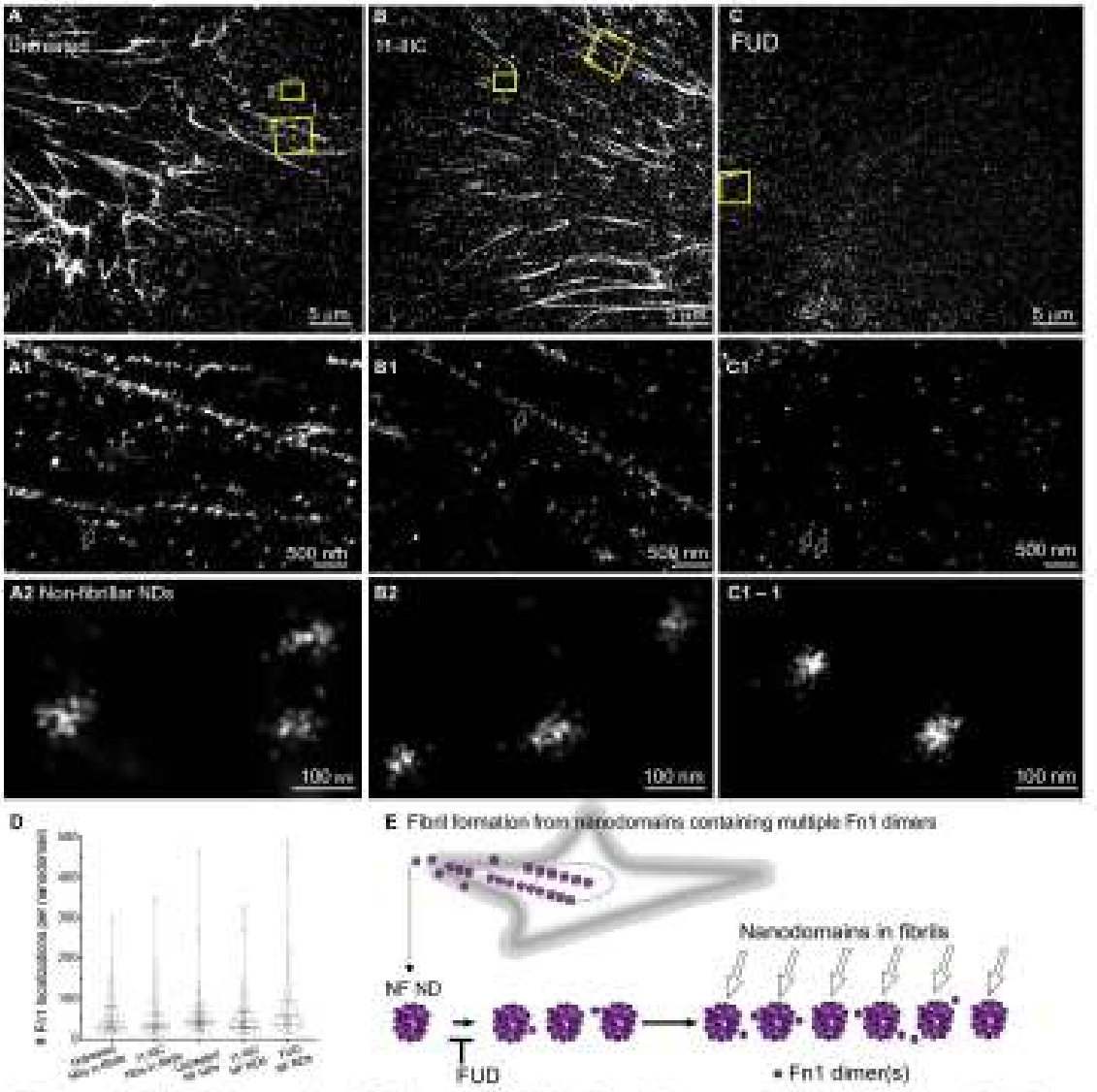

Figure 6. The N-terminal Fn1 assembly domain regulates the organization of Fn1 nanodomains into linear fibrillar arrays. $Fn1^{mEGFP/+}$ MEFs were plated on glass and were either left untreated, or were incubated with the control 11-IIIC peptide, or the FUD peptide for 16 hrs. Cell were then fixed and stained with the monoclonal antibody to Fn1 followed by Alexa 647-conjugated secondary antibodies. Cells were imaged at the critical angle of incidence by STORM. **A – A2**. Untreated, unpermeabilized cells. **B – B2.** Cells incubated with controls 11-IIIC peptide. **C – C1, C1-1** FUD-treated, unpermeabilized cells. Boxes marked 1 in **A-B** were expanded in **A1-B1**. Boxes marked 2 in **A-B**, were expanded in **A2 – B2**. The box in **C** is expanded in **C1** and **C1-1**. Arrows in **A1-B1** point to Fn1 nanodomains (NDs) in fibrils. Arrows in **C1** points to non-fibrillar nanodomains expanded in **C1-1**; **D.** Quantification of the number of Fn1 localizations in NDs in fibrils and in non-fibrillar NDs after various conditions. Red lines mark medians. Differences are not statistically significant, Kruskal-Wallis test with Dunn's correction for multiple testing. **E.** Model of fibril formation: Fn1 dimers assemble into small nanodomains containing integrin $\alpha5\beta1$ at cell periphery, move rearward with actin flow, and become organized into linear arrays of nanodomains. Joining of the additional Fn1 nanodomains to these arrays leads to the generation of longer fibrils as the assembly moves toward the cell center. FUD does not interfere with the formation of Fn1 nanodomains. But instead, it blocks the organization of Fn1 nanodomains into linear arrays.